Quantum magnon conversion accompanying magnon antibunching

Yaqi Fan,[*] Jiahua Li,[†] and Ying Wu[‡]
School of Physics, Huazhong University of Science and Technology, Wuhan 430074, People's Republic of China

(Received 25 April 2024; accepted 6 August 2024; published 23 August 2024)

The implementation of quantum network made up of multiple nodes and channels needs to take advantage of hybrid quantum systems. So far, in the hybrid ferromagnet-superconductor quantum system, the establishment of the remote effective interactions based on the virtual photons exchange mediated by the microwave cavity mode has been experimentally confirmed, providing a physical basis for the implementation of the remote signal transfer from one node to another. In this work, we put forward a magnon-based hybrid quantum system consisting of two macroscopic spin subsystems [i.e., millimeter-diameter ferromagnetic yttrium-iron-garnet (YIG) spheres] and one transmon-type superconducting qubit, and show that the mechanism of the cavity-mediated remote magnon-mode intertalk is feasible for achieving microwave signal transfer, simultaneously accompanied by a transition from Poissonian to sub-Poissonian statistics. We find that by tuning the typical system parameters properly, even if there is a mismatch in magnon-mode frequencies or dissipation rates between the two YIG spheres, the microwave information transfer from one YIG sphere to another is still robust, where the signal output through another YIG sphere exhibits pronounced antibunching. In addition, the proposed hybrid quantum system possesses a robustness window against the dissipation rates of both the qubit and the two Kittel modes. The analytical calculations and numerical simulations are conducted under experimentally accessible conditions, and the consistency of the results attained by these two methods makes our research more credible. Physically, we notice that two conversion channels are opened. One channel comes from the linear coupling. The other is based on the nonlinear interaction, which also is the underlying mechanism responsible for nonclassical sub-Poissonian signal output.

DOI: 10.1103/PhysRevA.110.023725

I. INTRODUCTION

The efficient control, operation, and conversion of signals between different modes are crucial capabilities for highly integrated information architectures in the future, whose achievements may require the utilization of more innovative hybrid quantum systems [1,2], such as the hybrid cavity magnetic system [2–4]. In recent years, the high-quality ferromagnetic insulator, namely, yttrium iron garnet (YIG) with the chemical formula $Y_3Fe_5O_{12}$ [5–8], emerges and attracts a great deal of attention due to its significant advantages, including the extremely low magnon dissipation rate with Gilbert damping factor down to 10^{-5} [9–11], the high order of magnitude of the spin density ($\sim 4.22 \times 10^{27}$ m^{-3}) [11,12], and the small mode volume [13,14], etc. YIG sphere can be regarded as a huge spin [14,15], providing the flexibility to be individually manipulated in experiments [16,17]. For instance, the systems based on the magnons, i.e., the bosonic spin excitation from the magnetic YIG spheres [18,19], exhibit better frequency adjustability compared with the electromechanical and optoelectronic systems [20], which can be achieved by controlling the external magnetic field to adjust the frequency of the magnons [16,21–23] ranging from MHz to THz [19,24,25]. Additionally, owing to the interactions with phonons [17,26–29], optical photons [25,30,31], and microwave photons [5,11,12] via the magnetostrictive effect, the magneto-optical effect and the magnetic dipole interaction, respectively, the magnons show the excellent compatibility and become a favored candidate to carry information. Some advancements have already yielded valuable insights into the magnon-based hybrid quantum systems which offer a broad platform for exploring abundant magnon quantum effects and implementing complex information processing, such as the preparation of quantum squeezed states of the phonons and the magnons [28], the magnon exceptional point [32,33], the photon-magnon bipartite [34] or photon-phonon-magnon tripartite entanglement [20,26], the magnon-induced transparency [17,27,35], the manipulation of distant spin current [36], the generation of magnon Schrödinger cat state [37], the magnon-induced nonreciprocity [38–41], the frequency conversion between the microwave photons and the optical photons [30,42,43], etc.

Existing experimental and theoretical progresses [16,21–23,44,45] demonstrate that due to the high spin density and the low magnon dissipation rate, the strong or even ultrastrong photon-magnon coupling [11,12,46] can be realized in the microwave cavity experiments [11,44], including the cavity-mediated long-distance Jaynes-Cummings (JC) interaction between the magnon excitation and the superconducting qubit [16,21,22]. The key of implementing this intertalk mechanism is to couple both the magnon excitation and the qubit

[*]Contact author: yaqi_fan2023@126.com
[†]Contact author: huajia_li@163.com
[‡]Contact author: yingwu2@126.com

to the common microwave cavity mode which acts as the quantum bus [47–52]. Owing to the large cavity-magnon and cavity-qubit frequency detunings, the indirect interaction is established through exchanging the virtual photons from the microwave cavity mode rather than relying on the real photons, which can effectively avoid the losses caused by the microwave cavity. In addition, it is necessary to adjust the frequencies of both the magnon mode and the qubit to be nearly resonant, which makes the coherent manipulation of the microwave magnons possible [22]. It has been confirmed that the manipulation of the single-magnon state through exploiting the superconducting qubit becomes a promising approach [21,21,44]. Furthermore, thanks to the establishment of the remote effective coupling, the coherent transfer of the microwave signal may hold the potential to survive at macroscopic distances.

On the basis of the experimental advancements above [16,21,22], the initial proposal to investigate the generation of the magnon antibunching effect was put forward in Ref. [53]. Similar to the principles of the photon antibunching effect [54–59] and the phonon antibunching effect [60–62], the magnon antibunching effect [63–67], a pure magnon-based quantum phenomenon, follows the sub-Poissonian statistics. It reveals an interesting phenomenon that the excitation of the first magnon would prevent the excitation of the second one, which leads to the repulsive interaction between the two consecutively emitted magnons and the orderly emissions of the magnons one by one [67]. The extremely strong magnon antibunching effect is also known as the magnon blockade, which is used to prepare the single-magnon sources and is beneficial to achieve the quantum manipulation at the level of a single magnon. As a significant means of describing the statistical properties of the fields, the second-order correlation function [68] is utilized to distinguish the sub-Poissonian statistics, Poissonian statistics, and the super-Poissonian statistics, which correspond to the magnon blockade, the magnon coherent state, and the magnon tunneling [69], respectively.

Motivated by the microwave cavity experiments [11,16,21–23,44,45] involving the magnetic YIG spheres, here we demonstrate a magnon-based hybrid quantum system to implement the cavity-mediated remote microwave signal transfer which accompanies strong magnon antibunching effect (i.e., sub-Poissonian magnon-number statistics). In our proposed hybrid ferromagnet-superconductor architecture, both one transmon-type superconducting qubit and two macroscopic ferromagnetic YIG spheres are properly placed into a three-dimensional (3D) microwave cavity. Like Ref. [2], the uniformly magnetized YIG spheres only retain the dominant uniform magnetostatic mode, namely, the Kittel mode which is the simplest Walker mode. The qubit and the two Kittel modes are coupled to the common microwave cavity mode through the electric and magnetic dipole interactions, respectively, which requires us to position the qubit and the YIG spheres at the antinode of the intracavity electric and magnetic field, respectively. Under the condition of the large cavity-magnon and cavity-qubit frequency detunings, the adiabatic elimination of the microwave cavity mode allows the establishment of the effective interactions through the virtual photons excitation of the common cavity mode. Therefore, the long-range effective interactions exhibit significant spatial tunability. The YIG sphere driven by a weak driving field can serve as the excitation node, while the YIG sphere not driven can serve as the receiving node.

With current experimentally accessible parameters, through analytical calculations and numerical simulations of the mode conversion efficiency between the two Kittel modes, as well as the second-order correlation function of the undriven Kittel mode (i.e., the receiving node), we explore in detail the feasibility of the magnon-based hybrid quantum system in achieving the remote magnon mode conversion accompanying the typical antibunching behavior. And we find that there are two microwave-mediated channels, contributing to the magnon conversion. To be specific, one channel is to exploit the linear magnon-magnon coupling mediated by the microwave cavity. The other is based on the nonlinear magnon-qubit interaction mediated by the microwave cavity. At the same time, the latter nonlinear interaction also gives rise to a classical-to-quantum crossover from the signal input to output, i.e., a Poisson-to-sub-Poisson transition. Our study has potential applications in preparing the long-distance microwave signal converter between the spatially separated macroscopic individuals, which provides the possibility for the ferromagnetic material YIG sphere to serve as a key node in the integrated quantum networks.

The remaining paper is organized according to the following arrangement. In Sec. II, we provide a detailed introduction of our theoretical model. And on the basis of the original Hamiltonian which includes the cavity-qubit and cavity-magnon couplings, we successfully derive an effective Hamiltonian which includes the long-range effective qubit-magnon and magnon-magnon couplings. In Secs. III A–III C, under the weak-driving limit, the analytical calculations of the mode conversion efficiency governed by the quantum Heisenberg-Langevin equation of motion and the zero-delay second-order correlation function of the undriven Kittel mode given by the Schrödinger equation are provided. In Sec. III D, we introduce the quantum master equation to investigate more accurate numerical results of the mode conversion efficiency and the zero-delay second-order correlation function of the undriven Kittel mode. Moreover, we compare the analytical solutions with the numerical results to confirm the consistency of these two methods, which can make our results more credible. In Sec. IV, the feasibility of the experimental implementation is briefly elaborated, and the system parameters are taken to the suitable values executed in actual experiments. In Sec. V, by adjusting typical system parameters, the mode conversion efficiency and the statistical characteristics of the magnons are discussed in detail. Finally, the results of our work are summarized and presented in Sec. VI. In Appendix A, we provide the validity of the ground-state approximation under the weak-driving condition from a numerical perspective. In order to make the main text more concise while maintaining the completeness of the content, the specific processes of analytically solving the Schrödinger equation are presented in Appendix C. In Appendixes B and D, we investigate the influence of the driving strength and the ambient temperature on the magnon conversion efficiency and the magnon antibunching effect, respectively.

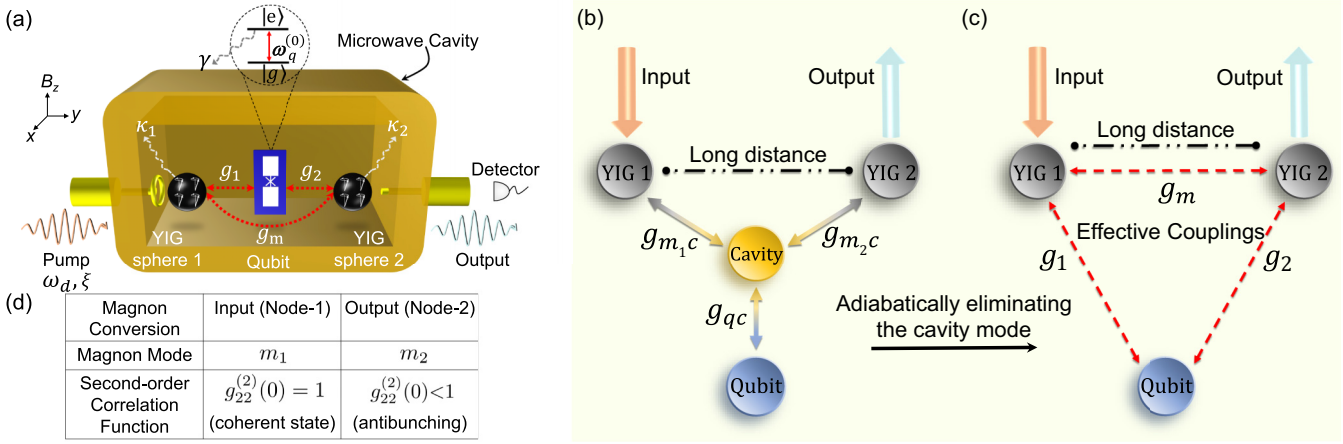

(d)

Magnon Conversion	Input (Node-1)	Output (Node-2)
Magnon Mode	m_1	m_2
Second-order Correlation Function	$g_{22}^{(2)}(0)=1$ (coherent state)	$g_{22}^{(2)}(0)<1$ (antibunching)

FIG. 1. (a) Schematic diagram of the proposed magnon-based superconducting qubit hybrid quantum system comprised of one transmon-type superconducting qubit and two millimeter-sized ferromagnetic YIG spheres. On the far left side of this panel, there is a loop antenna for loading the microwave driving field and pumping the adjoining YIG sphere 1 [70,77]. And the classical coherent laser is characterized by the carrier frequency ω_d and the driving strength ξ. On the far right of this panel, there is a detector used to detect the output magnons from the YIG sphere 2. g_i $(i=1,2)$ describes the magnon-qubit coupling strength of the ith Kittel mode to the qubit (i.e., the red straight dotted arrows). g_m depicts the magnon-magnon coupling strength between the two Kittel modes (i.e., the red curved dotted arrow). The x, y, and z directions of the 3D microwave cavity are marked in the upper left corner, and the direction of the magnetic field B_z which is used to uniformly magnetize the YIG spheres is along the z axis [12]. At the top of this panel, the inset encircled by the dashed circle box represents the energy-level diagram of the two-level qubit. The red solid double arrow denotes the transition between the ground state $|g\rangle$ and the excited state $|e\rangle$ of the qubit with the bare qubit transition frequency $\omega_q^{(0)}$ and dissipation rate γ [2,71]. (b) Schematic illustration of the original interactions in the hybrid quantum system. The microwave cavity mode can directly couple with the two Kittel modes and the qubit through the magnetic and electric dipole interactions, respectively, which are represented by these two-color solid arrows. g_{m_ic} (g_{qc}) denotes the magnetic (electric) dipole coupling strength of the ith Kittel mode (the qubit) to the microwave cavity mode. (c) Schematic representation of the remote effective interactions in the hybrid quantum system. The red dashed arrows describe the cavity-mediated long-range effective magnon-magnon and magnon-qubit couplings. Note that the input signal, denoted by the orange cylindrical arrows with the word "Input," is exactly resonant with the first Kittel mode. The light green cylindrical arrows with the word "Output" stand for the output magnon flux from the second Kittel mode. (d) The differences between the input signal and the output signal of this hybrid quantum system in terms of the magnon mode and the statistical properties characterized by the normalized second-order correlation function.

II. MODEL AND HAMILTONIAN

The simplified schematic diagram of the hybrid ferromagnet-superconductor quantum system under investigation is provided in Fig. 1(a). In the scheme considered here, there is one superconducting qubit and two spatially separated YIG spheres, all of which need to be positioned in a rectangular 3D microwave cavity at the same time. The YIG spheres (the qubit), which are placed near the magnetic-field (electric-field) antinode [44] of the microwave cavity mode, can establish direct cavity-magnon (cavity-qubit) interactions. As a consequence, the original Hamiltonian of the hybrid quantum system can be written with two parts (assuming $\hbar=1$ here and hereafter): one part is the original free Hamiltonian

$$\hat{H}_0^{(0)}=\omega_c\hat{c}^\dagger\hat{c}+\omega_q^{(0)}\hat{\sigma}^\dagger\hat{\sigma}+\sum_{i=1,2}\omega_{m_i}^{(0)}\hat{m}_i^\dagger\hat{m}_i, \tag{1}$$

which represents the total free energies of the microwave cavity mode, the qubit, and the two Kittel modes; and the other part is the original interaction Hamiltonian

$$\hat{H}_{\rm I}^{(0)}=g_{qc}\hat{\sigma}^\dagger\hat{c}+\sum_{i=1,2}g_{m_ic}\hat{m}_i^\dagger\hat{c}+{\rm H.c.} \tag{2}$$

There are some symbols that are necessary to be explained: the microwave cavity-mode frequency is denoted by ω_c, the bare frequency of the qubit is represented by $\omega_q^{(0)}$, and the bare frequency of the ith $(i=1,2)$ Kittel mode is indicated by $\omega_{m_i}^{(0)}$ which can be controlled by adjusting the amplitude of the local external magnetic field [not shown in Fig. 1(a)] [70]. H.c. means the Hermitian conjugate. The symbols $\hat{c}$ and $\hat{c}^\dagger$ correspond to the annihilation and creation operators of the microwave cavity mode. The transmon-type qubit can be described as an anharmonic oscillator [51]. Due to the strong anharmonicity in the considered qubit, it is reasonable to neglect the higher-energy levels and only consider the lowest two levels (i.e., the ground state and the first excited state) of the anharmonic oscillator as the qubit subspace [22]. Thus, $\hat{\sigma}=|g\rangle\langle e|$ and $\hat{\sigma}^\dagger=|e\rangle\langle g|$ are the excitonic lowering and raising operators between the ground state $|g\rangle$ and the first excited state $|e\rangle$ of the qubit in the inset of Fig. 1(a). The operator $\hat{m}_i^\dagger$ $(\hat{m}_i)$ can create (annihilate) an excitation in the uniformly precessing Kittel mode of the ith YIG sphere, and satisfies the usual bosonic commutation relation $[\hat{m}_i,\hat{m}_{i'}^\dagger]=\delta_{ii'}$ $(i,i'=1,2)$. The symbol g_{m_ic} (g_{qc}) stands for the direct coupling strength between the ith Kittel mode (the qubit) and the microwave cavity mode, i.e., the magnetic (electric) dipole coupling strength. For clarity, Fig. 1(b) provides a concise diagram to illustrate these original interactions. Owing to the

sufficient spatial separations among the qubit and the two magnetic YIG spheres, the direct interactions among them, which are not shown in Fig. 1(b), are so weak that they can be reasonably overlooked [14,44,71]. And such an operation is also adopted in the relevant experiments [16,22,44].

The original Hamiltonian involving the microwave cavity mode does not provide intuitive interactions among the two Kittel modes and the qubit, which is not conducive to gaining more insight into the information transfer among them. Now, we define the frequency detuning between the ith Kittel mode (the qubit) and the microwave cavity mode as $\delta_{ic} = \omega_{m_i}^{(0)} - \omega_c$ ($\delta_{qc} = \omega_q^{(0)} - \omega_c$). When the two Kittel modes and the qubit are nearly resonant with each other but far detuned from the microwave cavity mode, i.e., $|\omega_{m_i}^{(0)} - \omega_q| \ll \{g_{m_i c}$ and $g_{qc}\} \ll \{\delta_{ic}$ and $\delta_{qc}\}$ $(i = 1, 2)$ [72], it is feasible to use a Fröhlich-Nakajima transformation [73,74] to adiabatically eliminate the microwave cavity mode and derive the effective interactions which are described by the JC-type Hamiltonian. To be specific, we can consider a unitary transformation $\hat{U}_0 = e^{\hat{S}}$, where

$$\hat{S} = \frac{g_{m_1 c}}{\delta_{1c}}(\hat{c}^\dagger \hat{m}_1 - \hat{c}\hat{m}_1^\dagger) + \frac{g_{m_2 c}}{\delta_{2c}}(\hat{c}^\dagger \hat{m}_2 - \hat{c}\hat{m}_2^\dagger) + \frac{g_{qc}}{\delta_{qc}}(\hat{c}^\dagger \hat{\sigma} - \hat{c}\hat{\sigma}^\dagger) \tag{3}$$

is anti-Hermitian and needs to satisfy the constraint relationship $\hat{H}_{\rm I}^{(0)} + [\hat{H}_0^{(0)}, \hat{S}] = 0$ [75]. So the effective Hamiltonian $\hat{H}_{\rm eff} = \hat{U}_0^\dagger(\hat{H}_0^{(0)} + \hat{H}_{\rm I}^{(0)})\hat{U}_0$, which is only expanded to the second order [76], can be approximately expressed as

$$\begin{aligned}\hat{H}_{\rm eff} &\approx \hat{H}_0^{(0)} + \frac{1}{2}\big[\hat{H}_{\rm I}^{(0)}, \hat{S}\big] \\ &= \omega_q \hat{\sigma}^\dagger \hat{\sigma} + \sum_{i=1,2}[\omega_{m_i}\hat{m}_i^\dagger \hat{m}_i + g_i(\hat{m}_i^\dagger \hat{\sigma} + \hat{m}_i \hat{\sigma}^\dagger)] \\ &\quad + g_m(\hat{m}_1^\dagger \hat{m}_2 + \hat{m}_1 \hat{m}_2^\dagger),\end{aligned} \tag{4}$$

where $\omega_q = \omega_q^{(0)} + \frac{g_{qc}^2}{\delta_{qc}}$ and $\omega_{m_i} = \omega_{m_i}^{(0)} + \frac{g_{m_i c}^2}{\delta_{ic}}$ imply the effective frequencies of the qubit and the ith Kittel mode, respectively. It is clear that owing to the coupling to the microwave cavity mode, the qubit frequency ω_q (the ith magnon-mode frequency ω_{m_i}) is shifted by $\frac{g_{qc}^2}{\delta_{qc}}$ ($\frac{g_{m_i c}^2}{\delta_{ic}}$) from $\omega_q^{(0)}$ ($\omega_{m_i}^{(0)}$) [22]. $g_i = \frac{1}{2}g_{m_i c}g_{qc}(\frac{1}{\delta_{ic}} + \frac{1}{\delta_{qc}})$ means the remote effective magnon-qubit coupling strength between the ith Kittel mode and the qubit. $g_m = \frac{1}{2}g_{m_1 c}g_{m_2 c}(\frac{1}{\delta_{1c}} + \frac{1}{\delta_{2c}})$ denotes the remote effective magnon-magnon coupling strength. Therefore, the quanta of excitations are exchanged between the ith Kittel mode and the qubit at a rate which is proportional to the magnon-qubit coupling strength g_i [2]. Similarly, the quanta of excitations can also be exchanged between the two Kittel modes at a rate which is proportional to the magnon-magnon coupling strength g_m. Besides, it is obvious that by modulating the original cavity-magnon and cavity-qubit coupling strengths, the long-range effective coupling strengths can be controlled. Figure 1(c) shows a clear diagram to illustrate these effective interactions. Due to the significant frequency detunings between the microwave cavity mode and the two Kittel modes as well as the qubit, the microwave cavity mode can be reasonably regarded as always remaining in the ground state, i.e., $\langle \hat{c}^\dagger \hat{c} \rangle \approx 0$ [75], so that the microwave cavity mode can be adiabatically eliminated and the original Hamiltonian can also be greatly simplified.

The physical essence behind the intertalk among the two magnetic YIG spheres and the qubit is the generation and disappearance of the virtual photons from the microwave cavity mode [78]. That is to say, the microwave cavity mode provides a channel as the quantum bus to assist the exchange of the virtual photons among the two YIG spheres and the qubit [79]. Such a mechanism can offer tremendous insights into the remote information transfer between the indirectly interacting macroscopic magnets which have the potential to become an available node in the large-scale quantum networks.

Before proceeding further, there are four points we would like to emphasize about the transformation from Eqs. (1) and (2) to (4): (i) Because there is no direct interaction among the two Kittel modes and the qubit in Fig. 1(b), the microwave signal from one YIG node cannot be directly transferred to another. (ii) Due to the large frequency mismatch, the two Kittel modes and the qubit can not exchange the real photons but the virtual photons with the microwave cavity mode. Additionally, it is necessary to adjust the local external magnetic fields to tune the frequencies of the two Kittel modes [70] to be as close as possible to the frequency of the qubit. Based on the cavity-mediated long-distance JC interactions in Fig. 1(c), the second Kittel mode, which does not directly couple with the input laser field and the first Kittel mode, can obtain light from the first Kittel mode and the qubit. In other words, the microwave signal can be indirectly transferred from one YIG node to another. (iii) Compared with the negligible direct interactions among the two Kittel modes and the qubit which are very weak, the remote magnon-magnon and magnon-qubit couplings are strong. (iv) Unlike the real photons, the virtual photons have the advantages of nonradiation and nonpropagation [51], which can avoid the cavity-induced loss [78]. This is crucial because it implies that the cavity-mediated information transfer over such long distances is advantageous.

Below, we apply a microwave field to drive the first Kittel mode with the driving frequency ω_d and driving strength ξ, that is to say, we can read the driving Hamiltonian as $\hat{H}_{\rm d} = \xi(\hat{m}_1^\dagger e^{-i\omega_d t} + \hat{m}_1 e^{i\omega_d t})$. Without loss of generality, ξ is considered to be a real number. For the convenience of description, we define the Hamiltonian of the hybrid quantum system as the symbol $\hat{H}_{\rm sys} = \hat{H}_{\rm eff} + \hat{H}_{\rm d}$. In order to reduce the complexity of the subsequent computations caused by the dependence of the driving Hamiltonian $\hat{H}_{\rm d}$ on the time, the Hamiltonian $\hat{H}_{\rm sys}$ need to be switched into a rotating reference frame with respect to the driving field frequency ω_d. Under the help of the unitary transformation formula, namely,

$$\hat{H}_{\rm rot} = \hat{U}(t)\hat{H}_{\rm sys}\hat{U}^\dagger(t) - i\hat{U}^\dagger(t)\frac{\partial \hat{U}(t)}{\partial t}, \tag{5}$$

where $\hat{U}(t) = e^{-i\omega_d t(\hat{m}_1^\dagger \hat{m}_1 + \hat{m}_2^\dagger \hat{m}_2 + \hat{\sigma}^\dagger \hat{\sigma})}$ is a time-dependent unitary operator, a time-independent Hamiltonian describing the hybrid quantum system in the interaction picture can be

attained and written as

$$\hat{H}_{\rm rot} = \Delta_q \hat{\sigma}^\dagger \hat{\sigma} + \sum_{i=1,2} [\Delta_i \hat{m}_i^\dagger \hat{m}_i + g_i(\hat{m}_i^\dagger \hat{\sigma} + \hat{m}_i \hat{\sigma}^\dagger)] + g_m(\hat{m}_1^\dagger \hat{m}_2 + \hat{m}_1 \hat{m}_2^\dagger) + \xi(\hat{m}_1^\dagger + \hat{m}_1). \quad (6)$$

Here, $\Delta_1 = \omega_{m_1} - \omega_d$, $\Delta_2 = \Delta_1 + \delta_m$, and $\Delta_q = \Delta_1 + \delta_q$ are the driving detuning of the first Kittel mode, the second Kittel mode, and the qubit, respectively. The frequency detuning between the second Kittel mode (the qubit) and the first Kittel mode can be denoted by the symbol $\delta_m = \omega_{m_2} - \omega_{m_1}$ ($\delta_q = \omega_q - \omega_{m_1}$). On the basis of the quantum master equation for the density matrix, which incorporates Eq. (6), we perform the accurate numerical simulations which are presented in Sec. III D below.

In practical situations, the energy losses caused by the external environment are inevitable. As a consequence, it is necessary to take the dissipative process into consideration. The non-Hermitian Hamiltonian, which includes the influence of the dissipation terms, can be derived with the form

$$\hat{H}_{\rm tot} = \hat{H}_{\rm rot} - i\frac{\gamma}{2}\hat{\sigma}^\dagger \hat{\sigma} - \sum_{i=1,2} i\frac{\kappa_i}{2}\hat{m}_i^\dagger \hat{m}_i, \quad (7)$$

where γ accounts for the dissipation rate of the qubit and κ_i indicates the dissipation rate of the ith Kittel mode. The effective non-Hermitian Hamiltonian [i.e., Eq. (7)] offers us the approximate analytical results (presented in Secs. III A–III C below) which are governed by the Heisenberg-Langevin equation of motion and the Schrödinger equation of the wave function.

Finally, in order to gain a clearer understanding of the differences between the input signal and the output signal, we provide a brief diagram [i.e., Fig. 1(d)] to illustrate the differences. To be more specific, first of all, owing to the establishments of the remote effective couplings among the two Kittel modes and the qubit, the input microwave signal, which is exactly resonant with the first Kittel mode m_1 (i.e., $\Delta_1 = 0$), can be converted into the second Kittel mode m_2 which is not driven. That is, the magnon conversion from one node to another can survive over macroscopic distances via the cavity-mediated effective couplings. Second, with the aim of generating the nonclassical effects, the nonlinearity is required in the hybrid quantum system. The Josephson junctions providing the nonlinearity thus play an important role for the realization of the transmon-type qubit which can be modeled as an effective two-level system [22]. After utilizing a classical laser field to drive the first Kittel mode to the excited state, a single excitation can be transferred to the second Kittel mode, which is a feasible manipulation due to the nonlinearity of the qubit [2]. The input coherent light (i.e., the boundary between the classical and quantum states with the normalized second-order correlation function equal to unity) may be transferred into the antibunching microwave magnons (i.e., the quantum state with the normalized second-order correlation function less than unity). So our proposed hybrid quantum system has the potential to achieve the remote magnon-mode conversion accompanied by the sub-Poissonian signal output.

III. CALCULATIONS OF CONVERSION EFFICIENCY AND NORMALIZED ZERO-DELAY SECOND-ORDER CORRELATION FUNCTION UNDER WEAK-DRIVING SCENARIO

A. Magnon emission intensity by solving Heisenberg-Langevin equations of motion under weak-driving limit

Although the analytical calculations consider many approximations during the solving process, they are still an essential step in our research process because this approach provides a physically intuitive perspective. By substituting the non-Hermitian Hamiltonian [i.e., Eq. (7)] including the dissipation terms of the hybrid quantum system into the Heisenberg-Langevin equation of motion [80,81], i.e., $\frac{d\hat{\mathcal{A}}}{dt} = -i[\hat{\mathcal{A}}, \hat{H}_{\rm tot}]$, we can attain a set of differential equations of the operator $\hat{\mathcal{A}}$ ($\hat{\mathcal{A}} = \hat{m}_1$, $\hat{m}_2$, and $\hat{\sigma}$) as the form in the following:

$$\frac{dm_1}{dt} = -\left(i\Delta_1 + \frac{\kappa_1}{2}\right)m_1 - ig_1\sigma - ig_m m_2 - i\xi, \quad (8a)$$

$$\frac{dm_2}{dt} = -\left(i\Delta_2 + \frac{\kappa_2}{2}\right)m_2 - ig_2\sigma - ig_m m_1, \quad (8b)$$

$$\frac{d\sigma}{dt} = -\left(i\Delta_q + \frac{\gamma}{2}\right)\sigma + i(g_1 m_1 + g_2 m_2)\sigma_z. \quad (8c)$$

Here, due to the interest in the mean response of the proposed system, we replace all operators with their averages but, for simplicity, still use the same symbols. Additionally, in the cold reservoir limit, the noise terms also can be safely ignored, whose expected values are zero [81]. Besides, note that we use the factorization assumption, i.e., $\langle\hat{\mathcal{A}}\hat{\mathcal{B}}\rangle = \langle\hat{\mathcal{A}}\rangle\langle\hat{\mathcal{B}}\rangle$. By observing Eqs. (8a)–(8c), it is obvious that we do not obtain a closed set of equations for the first-order moments but the second-order moments, that is, the differential equation of σ [i.e., Eq. (8c)] is coupled to $m_1\sigma_z$ and $m_2\sigma_z$ [80].

Since our analytical calculations take the weak-driving condition into account, the qubit is mainly in the ground state $|g\rangle$, which means that it is reasonable to set the average value of σ_z to -1 [82,83]. To verify the rationality of this approximate operation, we provide the numerical simulation results in Appendix A. On the basis of such approximate operation above, the steady-state analytical solutions of the emission amplitudes of the two Kittel modes and the qubit are, respectively, yielded by

$$m_1 = -\frac{i\xi\left(a_2 a_q + g_2^2\right)}{a_1 a_2 a_q + a_1 g_2^2 + a_2 g_1^2 + a_q g_m^2 - 2ig_1 g_2 g_m}, \quad (9a)$$

$$m_2 = \frac{\xi(ig_1 g_2 - a_q g_m)}{a_1 a_2 a_q + a_1 g_2^2 + a_2 g_1^2 + a_q g_m^2 - 2ig_1 g_2 g_m}, \quad (9b)$$

$$\sigma = -\frac{\xi(a_2 g_1 - ig_2 g_m)}{a_1 a_2 a_q + a_1 g_2^2 + a_2 g_1^2 + a_q g_m^2 - 2ig_1 g_2 g_m}. \quad (9c)$$

Because we have made some approximations in the process of obtaining the above analytical solutions, which make the nonlinearity imperceptible intuitively, we will compare the approximate analytical solutions with the accurate numerical solutions in Sec. III D below.

B. Mode conversion efficiency of microwave magnons

It is necessary to provide a parameter to describe the efficiency of the long-distance information transfer between two spatially separated YIG spheres. In what follows, we define the microwave magnon-mode conversion efficiency η which quantifies how much magnon is transferred from the first Kittel mode with zero coupling to the second Kittel mode under the coupling, with the form

$$\eta = \frac{M_2}{M_0} = \frac{\kappa_2|m_2|^2}{\kappa_1|m_1|^2_{g_1=g_2=g_m=0}} = \frac{\kappa_2 a_1^2\left(g_1^2g_2^2 + a_q^2g_m^2\right)}{\kappa_1\left[\left(a_1a_2a_q + a_1g_2^2 + a_2g_1^2 + a_qg_m^2\right)^2 + 4g_1^2g_2^2g_m^2\right]}, \quad (10)$$

where

$$M_0 = \kappa_1|m_1|^2_{g_1=g_2=g_m=0} = \kappa_1\left|\frac{i\xi a_2a_q}{a_1a_2a_q}\right|^2 = \frac{\kappa_1\xi^2}{a_1^2}. \quad (11)$$

M_2 is the unnormalized output of the second Kittel mode. It should be noted that the denominator of the mode conversion efficiency, i.e., M_0, describes the integrated emission intensity of the first Kittel mode in the absence of the effective couplings [84] among the two Kittel modes and the qubit (i.e., $g_1 = g_2 = g_m = 0$) at $\Delta_1 = 0$. According to Ref. [84], the mode conversion efficiency can also be understood as the normalized average magnon population of the second Kittel mode, i.e., the normalized output magnon flux scattered from the second Kittel mode to the outside of the cavity [81]. In addition, we present the research on unnormalized average magnon population of the second Kittel mode in Appendix B.

By carefully investigating Eq. (10), it is not difficult to find that the output magnons of the second Kittel mode are composed of two parts which respectively correspond to two channels. More specifically, the first term of the numerator involves two effective coupling strengths, i.e., g_1 and g_2. That is to say, with the help of these two remote effective couplings, the microwave signal can be transferred from the excitation node (i.e., the first Kittel mode which is driven and resonant with the driving field) to the receiving node (i.e., the second Kittel mode which is not driven) with passing through the qubit. For convenience, this channel can be defined as channel I (the first Kittel mode $\xrightarrow{g_1}$ the qubit $\xrightarrow{g_2}$ the second Kittel mode). It is necessary to emphasize again that the channel I introduces nonlinearity due to the presence of the qubit, which was also mentioned in the analysis of Eq. (A1) in Appendix A. The second term of the numerator only involves one effective coupling strength, i.e., g_m. In other words, the microwave signal can be transferred from the excitation node (i.e., the first Kittel mode which is driven and resonant with the driving field) to the receiving node (i.e., the second Kittel mode which is not driven) without passing through the qubit. This channel can be defined as channel II (the first Kittel mode $\xrightarrow{g_m}$ the second Kittel mode) for the sake of convenience. Similarly, we need to point out that channel II does not introduce nonlinearity so that it can be seen as a linear channel.

In order to gain a clearer understanding of the competition between these two channels, we introduce a parameter T_x ($x = I, II$) which represents the ratio of the emission intensity of the channel x with respect to the total emission intensity of these two channels, namely,

$$T_I = \frac{g_1^2g_2^2}{g_1^2g_2^2 + a_q^2g_m^2} = \frac{g_{qc}^4}{g_{qc}^4 + a_q^2\delta_{qc}^2} = \frac{p^4g_{m_1c}^4}{p^4g_{m_1c}^4 + a_q^2\delta_{qc}^2} = \frac{1}{1 + \dfrac{a_q^2\delta_{qc}^2}{p^4g_{m_1c}^4}}, \quad (12a)$$

$$T_{II} = \frac{a_q^2g_m^2}{g_1^2g_2^2 + a_q^2g_m^2} = \frac{a_q^2\delta_{qc}^2}{g_{qc}^4 + a_q^2\delta_{qc}^2} = \frac{a_q^2\delta_{qc}^2}{p^4g_{m_1c}^4 + a_q^2\delta_{qc}^2} = \frac{1}{\dfrac{p^4g_{m_1c}^4}{a_q^2\delta_{qc}^2} + 1}, \quad (12b)$$

where we define the parameter p to denote the ratio of g_{qc} to g_{m_1c}, i.e., $p = g_{qc}/g_{m_1c}$. According to Eq. (12), we can easily discover that the parameter T_x is very sensitive to the cavity-qubit coupling strength g_{qc} and the dissipation of the qubit γ which is included in a_q, and so on. With the increase of the cavity-qubit coupling strength g_{qc}, the microwave signal tends to be transferred through channel I. Similarly, when we consider the two Kittel modes are resonant with the qubit, i.e., $\Delta_1 = \Delta_2 = \Delta_q = 0$ and $a_q = \gamma/2$, the microwave signal tends to be transferred through channel II with the increase of the qubit dissipation γ.

C. Insights into the normalized zero-delay second-order correlation function by solving Schrödinger equation under weak-driving scenario

As is well known, the magnon blockade effect is a typical magnon-based quantum effect and it can be seen as the counterpart of the photon blockade effect. It describes a nonclassical phenomenon that the excitation of the first magnon will block the excitation of the subsequent magnon. In what follows, we are interested in the quantum correlations among the output magnons of the second Kittel mode when only the first Kittel mode is driven. The normalized zero-delay second-order correlation function can be employed to evaluate the degree of the hindrance of the emitted magnon to the subsequent magnon emission and quantify the statistical properties of the output magnons. The expression of the normalized zero-delay second-order correlation function of the second Kittel mode can be written as

$$g_{22}^{(2)}(0) = \frac{\langle\Psi_{ss}|\hat{m}_2^{\dagger 2}\hat{m}_2^2|\Psi_{ss}\rangle}{\langle\Psi_{ss}|\hat{m}_2^{\dagger}\hat{m}_2|\Psi_{ss}\rangle^2}, \quad (13)$$

where Ψ_{ss} denotes the steady-state wave function and $\langle\Psi_{ss}|\hat{\mathcal{A}}|\Psi_{ss}\rangle$ is the ensemble average of the observable physical quantity $\hat{\mathcal{A}}$. Generally speaking, when the condition of $g_{22}^{(2)}(0) < 1$ is satisfied, the statistical characteristics of the magnons display the sub-Poissonian distribution, corresponding to the magnon antibunching effect which is a quantum effect of the magnons and represents that the excited magnons reduce the possibility of subsequent magnon excitation. If the value of $g_{22}^{(2)}(0)$ infinitely approaches zero, we can consider that a perfect single-magnon source is achieved. When the condition of $g_{22}^{(2)}(0) > 1$ is satisfied, the statistical

characteristics of the magnons display the super-Poissonian distribution, corresponding to the magnon bunching effect which is classical effect of the magnons and suggests that the excited magnons increase the possibility of subsequent magnon excitation. If the value of $g_{22}^{(2)}(0)$ exceeds two, the hybrid quantum system exhibits magnon superbunching effect [85]. Particularly, when the value of $g_{22}^{(2)}(0)$ equals to unity, the statistical characteristics of the magnons exhibit the Poisson distribution, corresponding to the coherent state which is the boundary between classical and quantum states.

For the goal of determining the analytical expression of the normalized zero-delay second-order correlation function of the output magnons from the second Kittel mode, it is necessary to explore the evolution of the wave function of the hybrid quantum system $|\Psi\rangle$, which is controlled and governed by the time-dependent Schrödinger equation, i.e., $i\frac{\partial|\Psi\rangle}{\partial t} = \hat{H}_{\rm tot}|\Psi\rangle$. We can expand the wave function $|\Psi\rangle$ into a direct product state, i.e., $|\alpha, m_1, m_2\rangle = |\alpha\rangle \otimes |m_1\rangle \otimes |m_2\rangle$, which denotes that the qubit is in the $|\alpha\rangle$ ($\alpha = g, e$) state, the magnon number of the first Kittel mode is m_1, and the magnon number of the second Kittel mode is m_2. Under the weak excitation condition, i.e., $\xi \ll \{\kappa_1, \kappa_2, \gamma, g_1, g_2 \text{ and } g_m\}$, the probabilities of the higher-order magnon number states being occupied are very small, so that the total excitation number can be safely truncated to not exceed two. The wave function $|\Psi\rangle$ thus can be approximately and reasonably expanded as

$$\begin{aligned}|\Psi\rangle \approx\ & C_{g00}|g,0,0\rangle + C_{g10}|g,1,0\rangle + C_{g01}|g,0,1\rangle + C_{g11}|g,1,1\rangle + C_{g20}|g,2,0\rangle + C_{g02}|g,0,2\rangle \\ & + C_{e00}|e,0,0\rangle + C_{e10}|e,1,0\rangle + C_{e01}|e,0,1\rangle,\end{aligned} \tag{14}$$

where the coefficient $C_{\alpha m_1 m_2}$ is the probability amplitude of the state $|\alpha, m_1, m_2\rangle$. Additionally, the different magnitudes between ξ and $\{\kappa_1, \kappa_2, \gamma, g_1, g_2, \text{and } g_m\}$ result in only a few energy levels being excited (as mentioned earlier, we perform the truncation operation on the wave function $|\Psi\rangle$), and most of the magnons and photons staying in the ground state $|g, 0, 0\rangle$. As a consequence, we can naturally get an approximate relationship which can be expressed as

$$|C_{g00}| \simeq 1 \gg \{|C_{g10}|, |C_{g01}|, |C_{e00}|\} \gg \{|C_{g11}|, |C_{g20}|, |C_{g02}|, |C_{e10}|, |C_{e01}|\}. \tag{15}$$

In order to obtain the analytical expressions of the probability amplitudes under the steady state, we substitute the non-Hermitian Hamiltonian [i.e., Eq. (7)] and the truncated wave function [i.e., Eq. (14)] into the Schrödinger equation (i.e., $i\frac{\partial|\Psi\rangle}{\partial t} = \hat{H}_{\rm tot}|\Psi\rangle$) which satisfies the steady-state condition $i\frac{\partial|\Psi\rangle}{\partial t} = 0$. For readability, the detailed derivation processes of solving the Schrödinger equation are provided in Appendix C. After iteratively calculating a closed set of algebraic equations [i.e., Eqs. (C2a)–(C2h) in Appendix C], we can attain the analytical expressions of the single-magnon excitation coefficient $C_{g01}^{\rm ss}$ and the two-magnon excitation coefficient $C_{g02}^{\rm ss}$ which are the main steady-state probability amplitudes responsible for the expression of $g_{22}^{(2)}(0)$. Thus, we only present the expressions of these two steady-state probability amplitudes as follows:

$$C_{g01}^{\rm ss} = \frac{(g_1 g_2 - g_m \Delta_q')\xi}{\Lambda}, \tag{16a}$$

$$C_{g02}^{\rm ss} = \frac{\left(g_1^4 g_2^2 - 2g_1^3 g_2 g_m \Delta_q' + 2g_1 g_2 g_m \chi_1 + g_m^2 \chi_2 + g_1^2 \chi_3\right)\xi^2}{\sqrt{2}\Lambda\left(\zeta_1 + 2g_1 g_2 g_m \zeta_2 + \Delta_1' \zeta_3 + g_m^2 \zeta_4 - g_1^2 \zeta_5\right)}, \tag{16b}$$

where some newly combined coefficients are introduced and defined by

$$\chi_1 = g_m^2 \Delta_q' - g_2^2(\Delta_2' + \Delta_q') + (\Delta_1' + \Delta_2')(\Delta_1' + \Delta_q')(\Delta_2' + \Delta_q'), \tag{17a}$$

$$\chi_2 = g_2^4 + g_2^2\left[\delta_q^2 + \delta_q \Delta_1' - \Delta_1'(\Delta_1' + \Delta_2')\right] - \Delta_q'(\Delta_1' + \Delta_2')\left[-g_m^2 + (\Delta_1' + \Delta_q')(\Delta_2' + \Delta_q')\right], \tag{17b}$$

$$\chi_3 = g_2^4 - g_2^2\left[g_m^2 + (\Delta_1' + \Delta_2')(\Delta_1' + \Delta_q')\right] - g_m^2\left[\delta_m^2 - (\delta_q - \Delta_1')(\Delta_1' + \Delta_q') + \delta_m(3\Delta_1' + \Delta_q')\right], \tag{17c}$$

$$\zeta_1 = -2g_1^3 g_2 g_m + g_1^4 \Delta_2' + g_m^4(\Delta_1' + \Delta_2'), \tag{17d}$$

$$\zeta_2 = -g_2^2 + g_m^2 + \delta_m(\delta_m + \delta_q) + 2(2\delta_m + \delta_q)\Delta_1' + 5\Delta_1'^2, \tag{17e}$$

$$\zeta_3 = \left[g_2^2 - (\Delta_1' + \Delta_2')(\Delta_1' + \Delta_q')\right]\left[g_2^2 - \Delta_2'(\Delta_2' + \Delta_q')\right], \tag{17f}$$

$$\zeta_4 = g_2^2 \delta_q - (\Delta_1' + \Delta_2')\left[\delta_q^2 + 4\delta_q \Delta_1' + 5\Delta_1'^2 + \delta_m(2\Delta_1' + \Delta_q')\right], \tag{17g}$$

$$\zeta_5 = g_m^2(\delta_m - \delta_q) - g_2^2(\Delta_1' + \Delta_2') + \Delta_2'\left[\delta_m^2 + 3\Delta_1'(\Delta_1' + \Delta_q') + \delta_m(3\Delta_1' + \Delta_q')\right], \tag{17h}$$

$$\Lambda = -2g_1 g_2 g_m + g_1^2 \Delta_2' + g_m^2 \Delta_q' + \Delta_1'\left(g_2^2 - \Delta_2' \Delta_q'\right). \tag{17i}$$

There are some symbols that need to be explained again: $\Delta_1' = \Delta_1 - i\frac{\kappa_1}{2}$, $\Delta_2' = \Delta_2 - i\frac{\kappa_2}{2}$, and $\Delta_q' = \Delta_q - i\frac{\gamma}{2}$. In order to make the main text more concise and easy to read, the expressions of the other steady-state probability amplitudes, whose contributions to the normalized zero-delay second-order correlation function of the second Kittel mode can be neglected, will no longer be shown and provided. So far, we complete the preparation work, that is, we successfully yield

the steady-state analytical solutions of the probability amplitudes $C^{\rm ss}_{g01}$ and $C^{\rm ss}_{g02}$ which are the core purpose of solving the Schrödinger equation.

Next, the above calculation results can be fully utilized to attain the analytical expression of the physical quantities of concern. After taking the truncated wave function [i.e., Eq. (14)] and the approximate relationship [i.e., Eq. (15)] above into consideration, the analytical expression of the normalized zero-delay second-order correlation function of the second Kittel mode thus can be simplified and expressed in terms of the steady-state coefficients $C^{\rm ss}_{\alpha m_1 m_2}$ as [68]

$$\begin{aligned} g^{(2)}_{22}(0) &= \frac{\langle\Psi_{\rm ss}|\hat{m}_2^{\dagger 2}\hat{m}_2^2|\Psi_{\rm ss}\rangle}{\langle\Psi_{\rm ss}|\hat{m}_2^{\dagger}\hat{m}_2|\Psi_{\rm ss}\rangle^2} \\ &= \frac{\sum_{\alpha,m_1,m_2} m_2(m_2-1)\left|C^{\rm ss}_{\alpha m_1 m_2}\right|^2}{\left(\sum_{\alpha,m_1,m_2} m_2\left|C^{\rm ss}_{\alpha m_1 m_2}\right|^2\right)^2} \\ &= \frac{2\left|C^{\rm ss}_{g02}\right|^2}{\left(\left|C^{\rm ss}_{g01}\right|^2+\left|C^{\rm ss}_{g11}\right|^2+2\left|C^{\rm ss}_{g02}\right|^2+\left|C^{\rm ss}_{e01}\right|^2\right)^2} \\ &\simeq \frac{2\left|C^{\rm ss}_{g02}\right|^2}{\left|C^{\rm ss}_{g01}\right|^4}, \end{aligned} \tag{18}$$

with the sum indices α and m_i being $\alpha = g, e$ and $m_i = 0, 1, 2$ $(i = 1, 2)$. Equation (18) clearly conveys a valuable message that indeed only the steady-state probability amplitudes $C^{\rm ss}_{g01}$ and $C^{\rm ss}_{g02}$ make a huge contribution to the normalized zero-delay second-order correlation function $g^{(2)}_{22}(0)$. By substituting Eqs. (16) and (17) into (18), we can obtain an analytical expression of the normalized zero-delay second-order correlation function $g^{(2)}_{22}(0)$ which is so bulky and complex that we cannot present it here.

The analytical calculations of the normalized zero-delay second-order correlation function $g^{(2)}_{22}(0)$ provide a method for us to better comprehend the magnon blockade effect from a mathematical perspective. By carefully observing the above-mentioned expression (19), it is not difficult to summarize that the perfect magnon blockade effect, i.e., $g^{(2)}_{22}(0) \approx 0$, which is the ultimate goal of our quest, can be achieved via setting the value of the coefficient $|C^{\rm ss}_{g02}|^2$ equal to zero. From a physical perspective, this is also reasonable. The occupying probability of the two-magnon state of the second Kittel mode is equal to zero, which implies that two magnons from the second Kittel mode cannot be excited simultaneously. Unfortunately, due to the complexity of the total Hamiltonian and the truncated wave function in our proposed hybrid quantum system, we cannot obtain an explicit expression of the optimal condition of achieving the magnon blockade effect so that it is difficult to offer more intuitive physical insights from a quantitative perspective. But it does not prevent us from analyzing the statistical properties of the second Kittel mode from a qualitative perspective. Through carefully looking into the steady-state probability amplitudes $C^{\rm ss}_{g01}$ and $C^{\rm ss}_{g02}$, we find that they are closely related to the cavity-magnon couplings, the cavity-qubit coupling, the magnon-magnon frequency detuning, and the dissipation rates of the two Kittel modes as well as the qubit, etc. This means that by the aid of the sensitive dependence of the magnon statistical properties on the typical system parameters, we can deeply explore the statistical properties of the magnons which will be displayed in more detail in Sec. V.

D. Dissipative dynamical evolution governed by quantum master equation

Another method to accurately elucidate the driving-dissipation characteristics of this hybrid quantum system is to solve the quantum master equation via using the numerical simulation methods. In this subsection, we conduct a detailed numerical calculation of the long-distance information transfer and the magnon statistical properties by utilizing the Lindblad quantum master equation. We assume a reservoir temperature of zero. Under the Born-Markovian approximation, the full quantum master equation is offered as [80,86,87]

$$\frac{d\hat{\rho}}{dt} = -i[\hat{H}_{\rm rot},\hat{\rho}] + \frac{\gamma}{2}\hat{\mathcal{L}}[\hat{\sigma}]\hat{\rho} + \sum_{i=1,2}\frac{\kappa_i}{2}\hat{\mathcal{L}}[\hat{m}_i]\hat{\rho}, \tag{19}$$

where the Hamiltonian $\hat{H}_{\rm rot}$ is given by Eq. (6) under the ω_d-rotating frame of the hybrid quantum system, γ denotes the dissipation rate of the qubit, and κ_i stands for the dissipation rate of the ith magnon mode. The last two terms can be expanded as the standard Lindblad type of the dissipation for the annihilation operator $\hat{\mathcal{A}}$ [$\hat{\mathcal{A}} = \hat{\sigma}$ and $\hat{m}_i$ $(i = 1, 2)$]. The Lindblad dissipation superoperator $\hat{\mathcal{L}}[\hat{\mathcal{A}}]$ acts on the density matrix $\hat{\rho}$, i.e., $\hat{\mathcal{L}}[\hat{\mathcal{A}}]\hat{\rho} = 2\hat{\mathcal{A}}\hat{\rho}\hat{\mathcal{A}}^\dagger - \hat{\mathcal{A}}^\dagger\hat{\mathcal{A}}\hat{\rho} - \hat{\rho}\hat{\mathcal{A}}^\dagger\hat{\mathcal{A}}$. These terms account for the losses to the environment.

When the evolution of the hybrid quantum system reaches a steady state which can be performed by solving Eq. (19) with the left hand set to zero, i.e., $\frac{d\hat{\rho}}{dt} = 0$, the steady-state magnon number of the mode $\hat{\mathcal{A}}$ satisfies $n^{\hat{\mathcal{A}}}_{\rm ss} = {\rm Tr}(\hat{\rho}_{\rm ss}\hat{\mathcal{A}}^\dagger\hat{\mathcal{A}})$, where $\hat{\rho}_{\rm ss}$ is the steady-state density matrix. Therefore, the normalized zero-delay second-order correlation function $g^{(2)}_{22}(0)$ of the second Kittel mode, which is a key physical quantity used to gain a physical insight into the magnon statistical characteristics, can be specifically yielded by [68]

$$g^{(2)}_{22}(0) = \frac{{\rm Tr}\left(\hat{\rho}_{\rm ss}\hat{m}_2^{\dagger 2}\hat{m}_2^2\right)}{[{\rm Tr}(\hat{\rho}_{\rm ss}\hat{m}_2^\dagger\hat{m}_2)]^2}, \tag{20}$$

where ${\rm Tr}(\dots)$ represents taking the trace operation. Similarly, the numerical expression of the magnon-mode conversion efficiency η can be written as

$$\eta = \frac{\kappa_2 n^{\hat{m}_2}_{\rm ss}}{\kappa_1 (n^{\hat{m}_1}_{\rm ss})_{g_1=g_2=g_m=0}} = \frac{\kappa_2 {\rm Tr}(\hat{\rho}_{\rm ss}\hat{m}_2^\dagger\hat{m}_2)}{\kappa_1 {\rm Tr}[\hat{\rho}_{\rm ss}(\hat{m}_1^\dagger\hat{m}_1)_{g_1=g_2=g_m=0}]}. \tag{21}$$

Additionally, in order to simulate the full quantum magnon conversion efficiency η and the normalized zero-delay second-order correlation function of the second Kittel mode $g^{(2)}_{22}(0)$ by using the PYTHON software, it is necessary to truncate the Hilbert space at a finite number of the magnons so that the full convergence can be guaranteed under the condition of the weak-driving scenario. To do so, we consider a Hilbert space expanded by the magnon Fock states of both Kittel modes and one qubit which is a two-level electronic system. The cutoff number of magnons as low as 10 for the two Kittel modes corresponds to a total Hilbert space of 200 for the

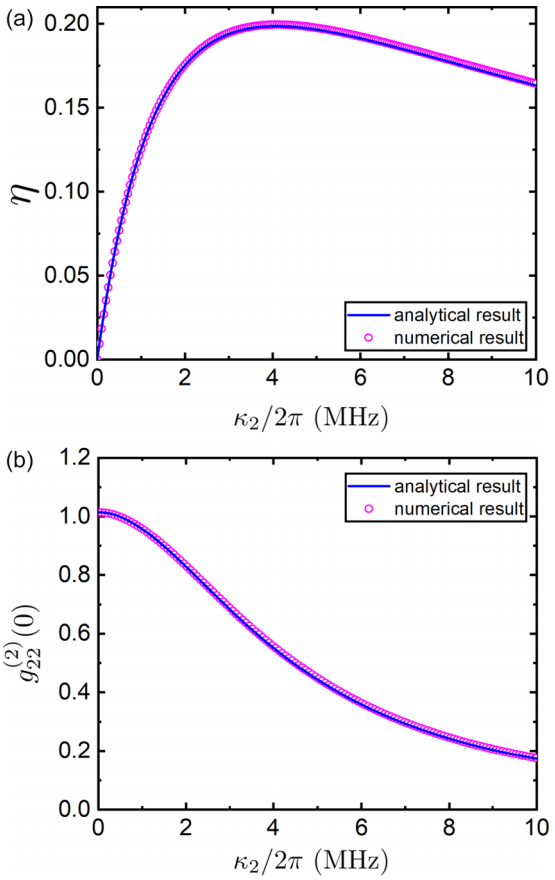

FIG. 2. Comparison between the analytical calculations (represented by the blue solid lines) and the numerical simulations (represented by the pink-circle lines) of the conversion efficiency η and the normalized zero-delay second-order correlation function of the second Kittel mode $g_{22}^{(2)}(0)$. (a) Conversion efficiency η varying with the dissipation rate of the second Kittel mode κ_2. (b) Normalized zero-delay second-order correlation function of the second Kittel mode $g_{22}^{(2)}(0)$ as a function of the dissipation rate of the second Kittel mode κ_2. The selections of the other system parameters used in these two plots are in accordance with the relevant experiments [16,21–23,44,45]: $\Delta_1 = \Delta_2 = \Delta_q = 0$ (i.e., $\delta_m = \delta_q = 0$), $g_{m_1c}/2\pi = 15$ MHz, $g_{m_2c}/g_{m_1c} = 1$, $g_{qc}/g_{m_1c} = 10$, $\xi/2\pi = 0.001$ MHz, $\kappa_1/2\pi = 5$ MHz, and $\gamma/2\pi = 1$ MHz.

hybrid quantum system. And such a master equation for the steady-state density matrix is equivalent to a linear system of 40 000 equations [88]. Hence, the truncated magnon number mentioned above is sufficient to guarantee the convergence of the simulations. The numerical simulations offered in this subsection and the analytical calculations offered in Sec. III C can provide us with a more comprehensive insight.

With the goal of verifying the correctness of the analytical results governed by the quantum Heisenberg-Langevin equation of motion and the Schrödinger equation, we compare the analytical results with the numerical results in the steady state. For example, the analytical solutions of the mode conversion efficiency η and the normalized zero-delay second-order correlation function of the second Kittel mode $g_{22}^{(2)}(0)$ are given by Eqs. (10) and (18), respectively, which are denoted by the blue solid lines in Fig. 2. And the numerical solutions of the mode conversion efficiency η and the normalized zero-delay second-order correlation function of the second Kittel mode $g_{22}^{(2)}(0)$ are expressed by Eqs. (21) and (20), respectively, which are indicated by the pink-circle lines in Fig. 2. We show the comparison between the analytical results and the numerical results under the weak-driving scenario. It is obvious that the analytical results can be faithfully reproduced by the numerical results. The consistency of the results attained from these two methods confirms the credibility of our results. For this reason, in the following main text, we will only present the numerical results obtained from the quantum master equation and the detailed results are given in Figs. 3–6 later.

IV. EXPERIMENTAL FEASIBILITY CONSIDERATION AND TYPICAL SYSTEM PARAMETER SELECTION

Before continuing the research, it is significant to briefly evaluate the experimental feasibility of the proposed hybrid quantum system. And based on the existing experiments, we can determine the appropriate values for the typical parameter involved in the implementation of our scheme. In accordance with the experimental reports in Refs. [16,21–23,44,45], at a considerably low temperature, both of the 1-mm-diameter YIG spheres need to be mounted in the oxygen-free copper part [12,21] of the 3D microwave cavity, and the transmon-type superconducting qubit needs to be mounted in the aluminum part [44] of the 3D microwave cavity. The reason for such placement and design is that the oxygen-free copper part cannot hinder the passage of the external magnetic field, making it convenient to control the frequencies of the two Kittel modes [23]. And in order to maintain the high coherence of the qubit and protect it from the disturbance of the magnetic field [22,44], it is necessary to ensconce the qubit in an aluminum space which exhibits diamagnetic and superconducting properties [23] at the extremely low temperature. Besides, this aluminum part also needs to be covered by a pure iron shell to achieve more efficient magnetic shielding [21]. In Appendix D, we explore the temperature limit of the considered hybrid quantum system for implementing the magnon-mode conversion accompanying the magnon antibunching effect, and compare this limit with relevant experimental works [16,22,23,44] to guarantee the experimental feasibility of the considered hybrid quantum system.

In the considered hybrid quantum system, the frequency of the microwave cavity mode TE_{102} is $\omega_c/2\pi = 8.653$ GHz; the transition frequency of the qubit which can be regarded as a two-level artificial atom [22,89,90] is $\omega_q/2\pi = 7.713$ GHz; and the uniform magnetostatic modes in ferromagnetic crystals possess tunable frequency ω_{m_i} $(i = 1, 2)$. By applying a uniform external bias magnetic field B_z to the YIG spheres, the YIG spheres can be magnetized to saturation and only retain the uniform magnetostatic modes [45] which are also known as the Kittel modes [2,16]. In addition, the two Kittel modes are also subject to the local magnetic fields [not shown in Fig. 1(a)] which are further applied to the two YIG spheres. Through tuning the amplitudes of the local external magnetic fields, the frequencies of the two Kittel modes can be controlled to be close to resonant with the qubit [70]. The resonant qubit and Kittel modes are far detuned from the microwave

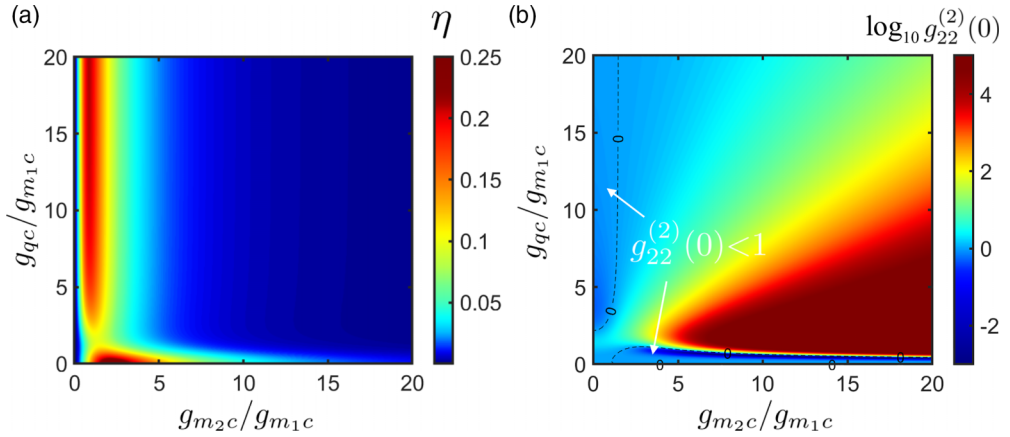

FIG. 3. (a) Contour map of the conversion efficiency η as a function of the ratio of the two cavity-magnon coupling strengths g_{m_2c}/g_{m_1c} as well as the ratio of the cavity-qubit coupling strength to the first cavity-magnon coupling strength g_{qc}/g_{m_1c}. (b) Contour map of the logarithmic normalized zero-delay second-order correlation function of the second Kittel mode $\log_{10} g_{22}^{(2)}(0)$ as a function of the ratio of the two cavity-magnon coupling strengths g_{m_2c}/g_{m_1c} as well as the ratio of the cavity-qubit coupling strength to the first cavity-magnon coupling strength g_{qc}/g_{m_1c}. The black dashed lines in (b) with label "0" are the contour of $\log_{10} g_{22}^{(2)}(0) \simeq 0$, i.e., $g_{22}^{(2)}(0) \simeq 1$. The white solid arrows with the label "$g_{22}^{(2)}(0) < 1$" point out the regions where the magnon antibunching effect can be achieved. The relevant system parameters used in these two contour maps are set to typical values which are borrowed from the advanced experimental progress [16,21–23,44,45]: $\Delta_1 = \Delta_2 = \Delta_q = 0$ (i.e., $\delta_m = \delta_q = 0$), $g_{m_1c}/2\pi = 15\,\mathrm{MHz}$, $\xi/2\pi = 0.001\,\mathrm{MHz}$, and $\kappa_1/2\pi = \kappa_2/2\pi = \gamma/2\pi = 1\,\mathrm{MHz}$.

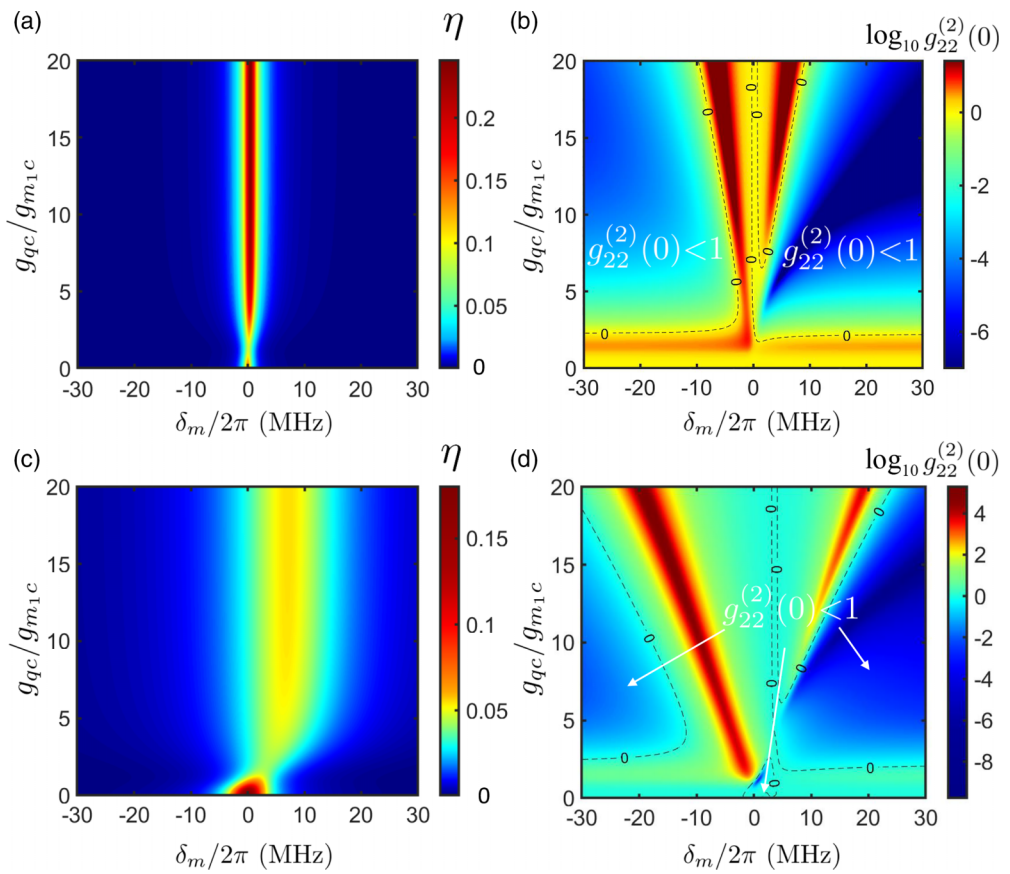

FIG. 4. Contour maps of the conversion efficiency η as a function of the frequency detuning between the two Kittel modes δ_m as well as the ratio of the cavity-qubit coupling strength to the first cavity-magnon coupling strength g_{qc}/g_{m_1c} for the parameters: $g_{m_2c}/g_{m_1c} = 1$ in (a) and $g_{m_2c}/g_{m_1c} = 4$ in (c). Contour maps of the logarithmic normalized zero-delay second-order correlation function of the second Kittel mode $\log_{10} g_{22}^{(2)}(0)$ as a function of the frequency detuning between the two Kittel modes δ_m as well as the ratio of the cavity-qubit coupling strength to the first cavity-magnon coupling strength g_{qc}/g_{m_1c} for the parameters $g_{m_2c}/g_{m_1c} = 1$ in (b) and $g_{m_2c}/g_{m_1c} = 4$ in (d). In (b) and (d), the black dashed lines with the label "0" and the white solid arrows with the label "$g_{22}^{(2)}(0) < 1$" have the same influence as those in Fig. 3(b). The values of the other parameters keep the same as those in Fig. 3.

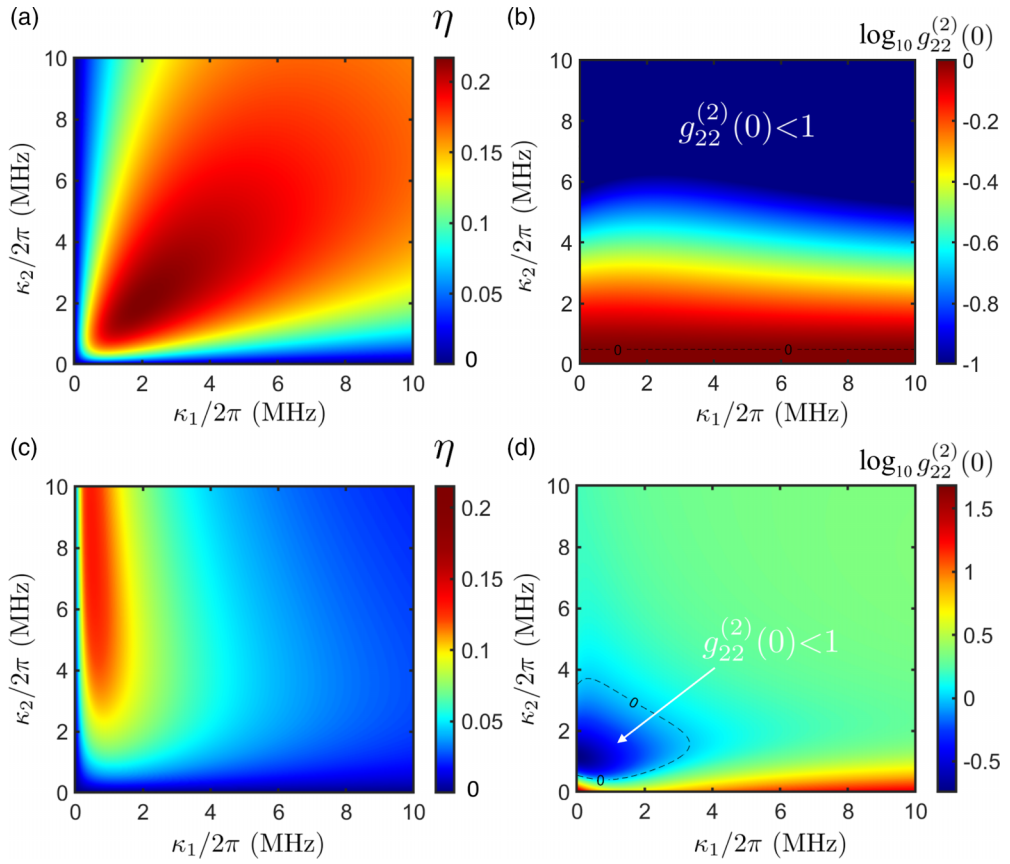

FIG. 5. Contour maps of the conversion efficiency η as a function of the dissipation rate of the first Kittel mode κ_1 as well as the dissipation rate of the second Kittel mode κ_2 for the parameters $g_{m_2c}/g_{m_1c} = 1$ with $g_{qc}/g_{m_1c} = 10$ in (a) and $g_{m_2c}/g_{m_1c} = 4$ with $g_{qc}/g_{m_1c} = 1$ in (c). Contour maps of the logarithmic normalized zero-delay second-order correlation function of the second Kittel mode $\log_{10} g_{22}^{(2)}(0)$ as a function of the dissipation rate of the first Kittel mode κ_1 as well as the dissipation rate of the second Kittel mode κ_2 for the parameters $g_{m_2c}/g_{m_1c} = 1$ with $g_{qc}/g_{m_1c} = 10$ in (b) and $g_{m_2c}/g_{m_1c} = 4$ with $g_{qc}/g_{m_1c} = 1$ in (d). In (b) and (d), the black dashed lines with label "0" are the contour of $\log_{10} g_{22}^{(2)}(0) \simeq 0$, i.e., $g_{22}^{(2)}(0) \simeq 1$. The values of the other parameters keep the same as those in Fig. 3.

cavity mode, which is a necessary experimental condition to achieve remote coherent couplings. Also, in Fig. 1(a), there is a specially designed port near the YIG sphere 1, and the end of this port is a loop antenna which can be used to load the microwave-driving field [70,77]. Finally, we would like to emphasize that because the electric field and magnetic field of the microwave cavity are located at the capacitive and inductive components, respectively, their antinodes can be easily spatially separated in the lumped-element cavity [2]. Our work brings the study of the hybrid cavity magnonics systems into the interesting remote-mode conversion.

On the basis of the experimental requirements mentioned above, we take reasonable values for the relevant system parameters which are allowed during the experimental implementation [16,21–23,44,45]. Due to the high spin density of the YIG magnets, the Kittel modes are coupled to the microwave cavity photons through the magnetic dipole interactions, whose strengths can reach strong or even ultrastrong coupling regions [11,12,46]. To this end, the YIG sphere 1, pumped by the weak driving field with strength $\xi/2\pi = 0.001$ MHz, needs to be placed near the magnetic-field antinode [44] of the microwave cavity mode TE_{102}. And the strength of the magnetic dipole interaction between the excited Kittel mode (from the YIG sphere 1) and the microwave cavity mode $g_{m_1c}/2\pi$ is 15 MHz. Similarly, the qubit needs to be placed near the electric-field antinode of the microwave cavity mode TE_{102}, and the strength of the electric dipole interaction between the qubit and the microwave cavity mode is g_{qc} with $p = g_{qc}/g_{m_1c}$. The undriven Kittel mode from the YIG sphere 2 couples with the microwave cavity mode through the magnetic dipole interaction g_{m_2c} with $d = g_{m_2c}/g_{m_1c}$. The Kittel-mode linewidths are taken to the value of $\kappa_1/2\pi = \kappa_2/2\pi = 1$ MHz. The dissipation rate of the qubit is set to the value of $\gamma/2\pi = 1$ MHz, too. Unless otherwise noted, we will always employ these typical values of the system parameters. Under different parameter conditions, the more in-depth results of numerical simulations via utilizing the quantum master-equation method are presented and discussed in the following chapter.

In addition, considering that the frequency of the magnon is in the microwave band [37], which represents that the energy of the microwave magnons is much lower than that of the optical photons, the common method of directly measuring the second-order correlation function by employing the Hanbury Brown–Twiss interferometer [91,92], becomes challenging and less suitable for the magnons [93]. The direct measurement of the second-order correlation function of the microwave photons in the circuit quantum electrodynamics

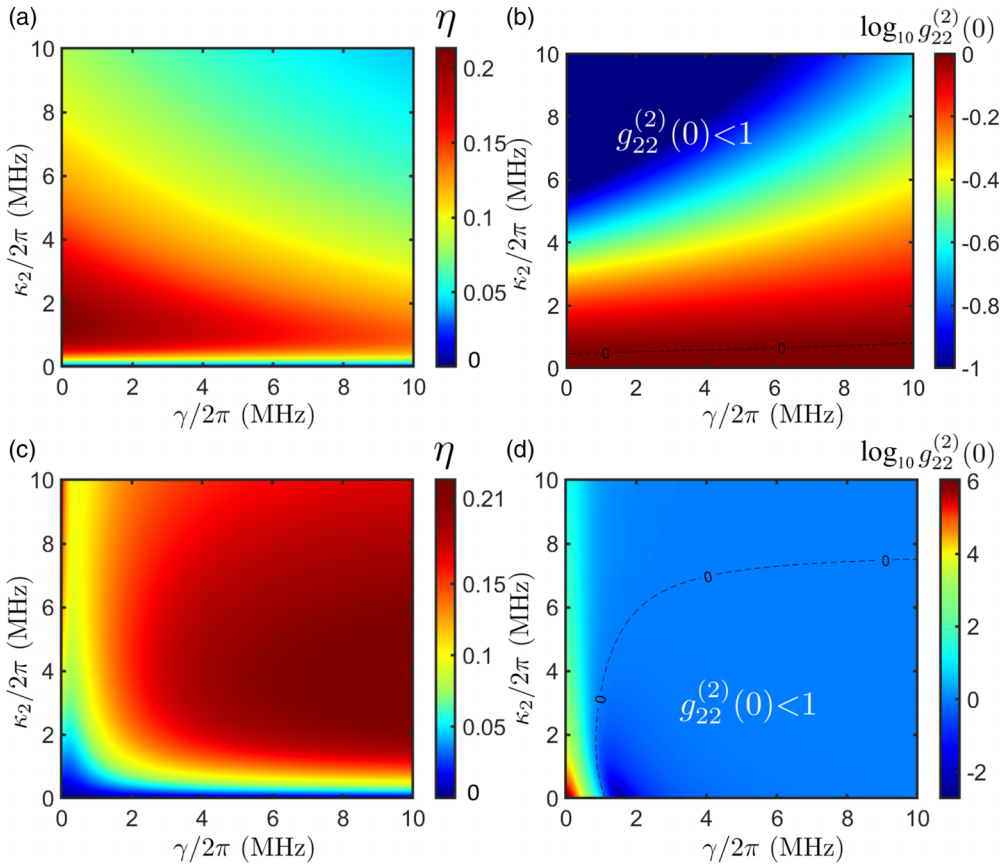

FIG. 6. Contour maps of the conversion efficiency η as a function of the dissipation rate of the qubit γ as well as the dissipation rate of the second Kittel mode κ_2 for the parameters $g_{m_2c}/g_{m_1c} = 1$ with $g_{qc}/g_{m_1c} = 10$ in (a) and $g_{m_2c}/g_{m_1c} = 4$ with $g_{qc}/g_{m_1c} = 1$ in (c). Contour maps of the logarithmic normalized zero-delay second-order correlation function of the second Kittel mode $\log_{10} g_{22}^{(2)}(0)$ as a function of the dissipation rate of the qubit γ as well as the dissipation rate of the second Kittel mode κ_2 for the parameters $g_{m_2c}/g_{m_1c} = 1$ with $g_{qc}/g_{m_1c} = 10$ in (b) and $g_{m_2c}/g_{m_1c} = 4$ with $g_{qc}/g_{m_1c} = 1$ in (d). In (b) and (d), the black dashed lines with label "0" are the contour of $\log_{10} g_{22}^{(2)}(0) \simeq 0$, i.e., $g_{22}^{(2)}(0) \simeq 1$. The values of the other parameters keep the same as those in Fig. 3.

(QED) systems has been achieved by using the measurement records of the linear detectors [93–95], rather than relying on the number or intensity detectors. We expect that the second-order correlation function of the microwave magnons can also be directly measured via utilizing the same experimental method which is presented in detail in Ref. [94].

V. RESULTS AND DISCUSSIONS ABOUT MAGNON CONVERSION ACCOMPANYING MAGNON ANTIBUNCHING EFFECT

For the sake of providing a meaningful parameter adjustment scheme, we fully consider the values of the qualitative analysis offered by the analytical solutions (10) and (18). Therefore, we plan to delve into the modulation effect of the typical system parameters on the conversion efficiency η and the normalized zero-delay second-order correlation function $g_{22}^{(2)}(0)$, e.g., the magnon-magnon frequency detuning δ_m, and the dissipation rates of the two Kittel modes κ_i $(i = 1, 2)$ as well as the qubit dissipation rate γ. Additionally, in the process of the numerical simulations and the result discussions, our focus is on the intuitive degrees of freedom that can be directly measured or manipulated in experiments, such as the original cavity-magnon coupling g_{m_ic} $(i = 1, 2)$ and the original cavity-qubit coupling g_{qc}, rather than the effective coupling strength g_i and g_m.

First, with the goal of gaining a better insight into the independent regulatory effect of the cavity-magnon coupling g_{m_2c} and the cavity-qubit coupling g_{qc} on the mode conversion and the magnon statistical properties, we assume that the two Kittel modes and the qubit have the same dissipation rate and effective frequency, that is, $\kappa_1 = \kappa_2 = \gamma$ and $\omega_{m_1} = \omega_{m_2} = \omega_q$ (i.e., $\delta_m = \delta_q = 0$). The conversion efficiency η and the logarithmic normalized zero-delay second-order correlation function $\log_{10} g_{22}^{(2)}(0)$ are computed to produce Figs. 3(a) and 3(b), respectively, which show the conversion efficiency η and the logarithmic normalized zero-delay second-order correlation function of the second Kittel mode $\log_{10} g_{22}^{(2)}(0)$ as a function of the ratio of the two cavity-magnon coupling strengths g_{m_2c}/g_{m_1c} as well as the ratio of the cavity-qubit coupling strength to the first cavity-magnon coupling strength g_{qc}/g_{m_1c}. In Fig. 3(a), in the center area where the values of g_{m_2c} and g_{qc} are comparable, the conversion of the magnon modes hardly occurs. However, it is obvious that the magnon mode conversion occurs in two regions, namely, the strong cavity-qubit coupling with the weak cavity-magnon coupling region, and the weak cavity-qubit coupling with the strong cavity-magnon coupling region. When we shift our

attention to the normalized zero-delay second-order correlation function of the second Kittel mode in Fig. 3(b), the contour lines of $\log_{10} g_{22}^{(2)}(0) \simeq 0$ are added in this panel which clearly distinguish the regions of the pure quantum regimes and the classical regimes [96]. We find that the parameter range that can generate the magnon antibunching effect highly overlaps with the parameter range that can achieve the magnon-mode conversion. Based on these attainable analyses, we can gain a preliminary conclusion that our proposed magnon-based hybrid quantum system indeed can achieve the remote signal transfer from one node to another accompanying the well-behaved sub-Poissonian character of the magnons emitted by the second Kittel mode. That is to say, we simultaneously implement the two transformations mentioned in Fig. 1(d).

It should be emphasized that when g_{qc} is equal to zero which leads to $g_i = 0$ $(i = 1, 2)$, i.e., the qubit does not participate in the remote signal transfer process, the output magnons of the second Kittel mode are in the coherent state [where the black dashed line partially overlaps with the x-coordinate axis in Fig. 3(b)]. In this case, the efficiency of mode conversion is still high, but it is a linear conversion. With the introduction of the qubit, i.e., g_{qc} is not equal zero, the output magnons of second Kittel mode exhibit significant magnon antibunching effect $[g_{22}^{(2)}(0) < 10^{-2}]$, which verifies that the qubit is very essential for achieving the magnon quantum effect.

According to what has been analyzed above, we discover that for the sake of achieving the mode conversion accompanied by the sub-Poissonian signal output simultaneously, we need to adjust the values of g_{qc} and g_{m_2c} to make them significantly different. On the basis of this condition, we plan to explore the regulatory effects of the other system parameters on the magnon-mode conversion efficiency η and the logarithmic normalized zero-delay second-order correlation function $\log_{10} g_{22}^{(2)}(0)$ under the premises of either $g_{m_2c}/g_{m_1c} = 1$ or $g_{m_2c}/g_{m_1c} = 4$.

In order to make our research more closely related to experimental reality, it is necessary to take the fact that we cannot obtain two YIG ferromagnetic samples with the same frequency in the experiments into account, i.e., $\delta_m \neq 0$. In Fig. 4, the two-dimensional color-scale maps of the conversion efficiency η and the logarithmic normalized zero-delay second-order correlation function $\log_{10} g_{22}^{(2)}(0)$ are plotted versus the frequency detuning between the two Kittel modes δ_m as well as the ratio of the cavity-qubit coupling strength to the first cavity-magnon coupling strength g_{qc}/g_{m_1c} simultaneously. In Figs. 4(a) and 4(b), g_{m_2c}/g_{m_1c} is assigned a smaller value, i.e., $g_{m_2c}/g_{m_1c} = 1$. When the frequency detuning between the two magnon modes is very small, the magnon-mode conversion can reach the maximum value 24.6%. We shift our focus on the logarithmic normalized zero-delay second-order correlation function of the second Kittel mode in Fig. 4(b). Unfortunately, under the same condition, the considered hybrid quantum system exhibits Poisson output. These results suggest that this parameter scheme is too strict for the two YIG ferromagnetic samples, which is not friendly and convenient to conduct experiments. So we need to adjust the other system parameters to achieve the magnon-mode conversion accompanied by the significant sub-Poissonian signal output. Besides, similar to Fig. 3(b), when g_{qc} is equal to zero, i.e., there is no qubit, the second Kittel mode cannot realize magnon antibunching effect. When g_{m_2c}/g_{m_1c} is assigned a larger value, i.e., $g_{m_2c}/g_{m_1c} = 4$ in Figs. 4(c) and 4(d), the regulation effect of δ_m and g_{qc}/g_{m_1c} on the output of the hybrid quantum system is improved. The parameter range, which can simultaneously realize the magnon-mode conversion and the sub-Poissonian signal output, is expanded. Within the region of the weaker cavity-qubit coupling strength and the smaller magnon-magnon frequency detuning, we can obtain the antibunching signal output with high magnon-mode conversion efficiency. With the increase of the magnon-magnon frequency detuning, the magnon-mode conversion efficiency begins to decrease. But within the same parameter range, the value of $g_{22}^{(2)}(0)$ can reach the negative second power of ten.

In the experimental implementation process, we cannot guarantee that the frequencies of the two Kittel modes are the same, nor can we guarantee that their dissipation rates are also the same. Consequently, the investigation of the mismatch between their dissipation rates is meaningful for the experiments. In Figs. 5(a) and 5(b), we plot the two-dimensional color-scale maps of the conversion efficiency η and the logarithmic normalized zero-delay second-order correlation function $\log_{10} g_{22}^{(2)}(0)$ as a function of the dissipation rate of the first Kittel mode κ_1 as well as the dissipation rate of the second Kittel mode κ_2 with $g_{m_2c}/g_{m_1c} = 1$ and $g_{qc}/g_{m_1c} = 10$. In Fig. 5(a), within the considered coordinate range, when the values of κ_1 and κ_2 are comparable, η, which approaches the maximum value ∼21%, shows the robustness against κ_1 and κ_2. In Fig. 5(b), within almost the entire parameter range, the value of $g_{22}^{(2)}(0)$ is less than unity all the time, representing that the output of the second Kittel mode is antibunching. And with the increase of κ_2, the value of $g_{22}^{(2)}(0)$ instead gradually decreases from unity, which provides us a way to control the smooth transition of the statistical characteristics of the output magnons for the second Kittel modes from Poissonian to sub-Poissonian. However, due to the bulky and complex analytical expression of $g_{22}^{(2)}(0)$ given by Eq. (18) which includes the high-order variables, we are unable to provide an intuitive physical explanation from a quantitative perspective for this monotonic behavior. Besides, the value of $g_{22}^{(2)}(0)$ is strongly robust against κ_1. In Figs. 5(c) and 5(d), the magnon-mode conversion and the magnon antibunching effect are demonstrated under the condition of $g_{m_2c}/g_{m_1c} = 4$ and $g_{qc}/g_{m_1c} = 1$. In Fig. 5(c), when the dissipation rate of the first Kittel mode κ_1 is low and the dissipation rate of the second Kittel mode κ_2 is large, the mode conversion efficiency η is high. However, the magnon antibunching effect is concentrated in the region of the low magnon dissipation rates. Compared with the results under the condition of $g_{m_2c}/g_{m_1c} = 1$ and $g_{qc}/g_{m_1c} = 10$, we cannot simultaneously achieve the magnon-mode conversion and the magnon antibunching effect in a large parameter space.

On the basis of the previous research results, it can be seen that the qubit plays an important role, so we are also curious about the regulatory effect of the qubit dissipation rate on the magnon-mode conversion and the magnon statistical properties. Figures 6(a) and 6(b) display the magnon-mode conversion efficiency η and the logarithm of the normalized zero-delay second-order correlation function $g_{22}^{(2)}(0)$, respectively, as a function of the dissipation rate of the qubit γ as

well as the dissipation rate of the second Kittel mode κ_2 with $g_{m_2c}/g_{m_1c} = 1$ and $g_{qc}/g_{m_1c} = 10$. In the region of the low qubit dissipation rate, although the value of the magnon dissipation rate κ_2 is large, the magnon mode conversion efficiency is still high. In the same parameter range, we can also generate the nonclassical output of the second Kittel mode, which is shown in Fig. 6(b). Besides, similar to the results of Fig. 5(b), within almost the entire parameter range, the value of $g_{22}^{(2)}(0)$ is less than unity all the time. Next, we still need to change the relative size of g_{m_2c} and g_{qc}, that is, we set $g_{m_2c}/g_{m_1c} = 4$ and $g_{qc}/g_{m_1c} = 1$ in Figs. 6(c) and 6(d). The region where the degree of the magnon-mode conversion is high overlaps with the region where the magnon antibunching effect can be achieved. And this region is far away from the low qubit dissipation region, which means that the proposed hybrid quantum system is very tolerant towards the qubit dissipation rate. Now, we can summarize that our system has strong robustness against the dissipation rates of both the two Kittel modes and the qubit, which provides us with more parameter selection freedom to realize the magnon-mode converter accompanied by the antibunching signal output.

VI. CONCLUSIONS

In summary, we demonstrate that in the proposed hybrid ferromagnet-superconductor quantum system consisting of one transmon-type superconducting qubit and two millimeter-sized ferromagnetic YIG spheres, the long-range microwave signal conversion can be realized between the two macroscopic magnets accompanying the sub-Poissonian signal output. Because of the large frequency mismatches between the microwave cavity mode and the magnon modes as well as the qubit, the microwave cavity mode can be regarded as a medium undertaking the virtual photons exchange and thus offer a physical basis for the realization of the remote effective magnon-qubit and magnon-magnon couplings which hold the advantage of the high spatial adjustability. Moreover, the introduction of the qubit provides us with the nonlinearity which is an essential condition for the achievement of the magnon quantum effects. Our displayed analytical calculations indicate that the undriven magnon mode (i.e., the second Kittel mode) can obtain the coherent microwave radiation with the assistance of the two conversion channels related to the effective couplings. The channel with the magnon-qubit couplings is a nonlinear channel, while the other channel without the magnon-qubit couplings is a linear channel.

Besides, we investigate the independent modulation effects of the cavity-magnon and cavity-qubit couplings on the mode conversion and the magnon statistical properties. It is found that only when the values of g_{m_2c} and g_{qc} are uncomparable, the microwave signal can be transferred from one YIG sphere to another, and the signal output through the latter node simultaneously exhibits significant antibunching effect. At the same time, our proposed scheme is robust over a large window of the dissipation rates of the magnon modes and the qubit, which means that even if the dissipation rates of the two Kittel modes are largely mismatched, it is still feasible and robust to use the two YIG spheres as the nodes to perform the microwave signal transfer, simultaneously accompanied by a transition from the Poissonian statistics to the sub-Poissonian statistics. Furthermore, we compare the approximate analytical results governed by the quantum Heisenberg-Langevin equation of motion and the Schrödinger equation with the accurate numerical simulations governed by the quantum master equation, finding that the agreement between these two methods is quite good. Our scheme is also feasible within the experimentally achievable temperature range. All the obtained results suggest that the possible applications of the proposed scheme include the preparation of the magnon-mode converters and the control of the statistical characteristics of the output microwave signal.

Finally, it is worth pointing out that, taking inspiration from the current work, it would be interesting to engineer a more complex magnon-based hybrid quantum system which contains more than two ferromagnetic YIG spheres. Mediated by a common microwave cavity mode, the qubit and these Kittel modes can establish remote effective couplings with each other. The only qubit that exists in the hybrid quantum system provides the necessary nonlinearity for the achievement of the quantum effects. After coherently driving one of the Kittel modes, the remote signal transfer among multiple magnetic nodes may be accompanied by more diverse statistical characteristics.

ACKNOWLEDGMENTS

We thank the two anonymous referees for constructive comments, which well improve our paper. We also acknowledge X. Yang for enlightening discussions. This research is supported partially by the National Natural Science Foundation of China (NSFC) through Grant No. 12275092 and by the National Key Research and Development Program of China under Contract No. 2021YFA1400700. The computation is completed in the HPC Platform of Huazhong University of Science and Technology.

APPENDIX A: VERIFICATION OF GROUND-STATE APPROXIMATION FROM ACCURATE NUMERICAL PERSPECTIVE

In Sec. III A, based on a set of differential equations of the hybrid quantum system, i.e., Eq. (8), the analytical expressions of m_1, m_2, and σ nested with σ_z can be obtained and written as

$$m_1 = -\frac{i\xi\left(a_2a_q - g_2^2\sigma_z\right)}{a_1a_2a_q + a_qg_m^2 - \sigma_z\left(a_1g_2^2 + a_2g_1^2 - 2ig_1g_2g_m\right)}, \tag{A1a}$$

$$m_2 = \frac{\xi(-ig_1g_2\sigma_z - a_qg_m)}{a_1a_2a_q + a_qg_m^2 - \sigma_z\left(a_1g_2^2 + a_2g_1^2 - 2ig_1g_2g_m\right)}, \tag{A1b}$$

$$\sigma = -\frac{\xi(ig_2g_m - a_2g_1)\sigma_z}{a_1a_2a_q + a_qg_m^2 - \sigma_z\left(a_1g_2^2 + a_2g_1^2 - 2ig_1g_2g_m\right)}, \tag{A1c}$$

where $a_1 = i\Delta_1 + \frac{\kappa_1}{2}$, $a_2 = i\Delta_2 + \frac{\kappa_2}{2}$, and $a_q = i\Delta_q + \frac{\gamma}{2}$. It is clear that σ_z always is multiplied by the terms involving g_1 or g_2, which provides nonlinearity for the interactions between the qubit and the two Kittel modes. In addition, $\hat{\sigma}_z$

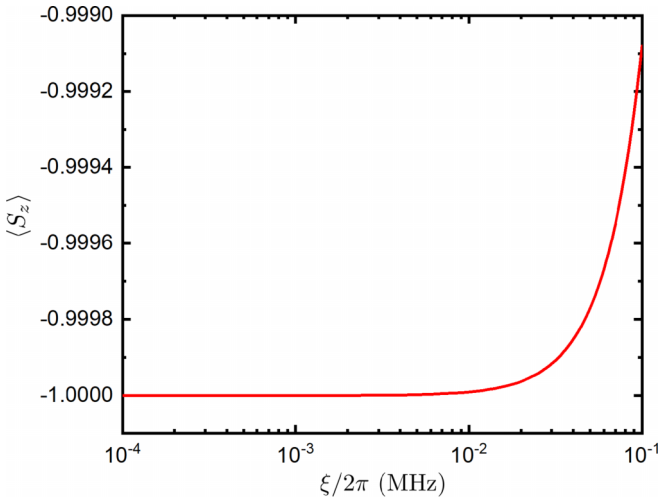

FIG. 7. Dependence of the average value of σ_z on the driving strength ξ. The values of the other parameters keep the same as those in Fig. 3, except for $g_{m_2c}/g_{m_1c} = 1$ and $g_{qc}/g_{m_1c} = 10$.

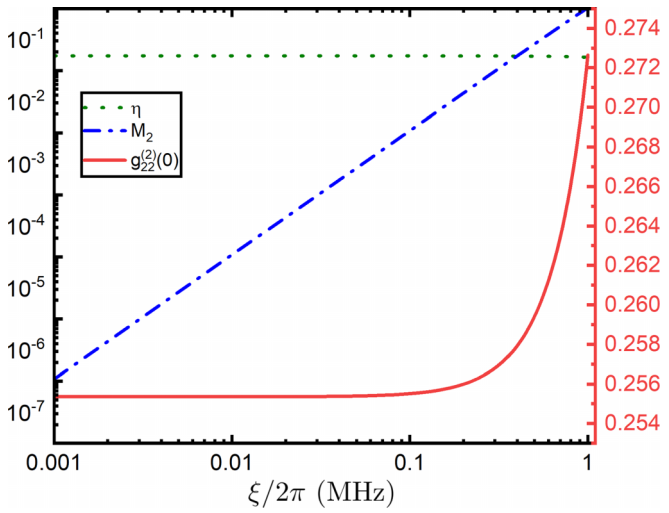

FIG. 8. Dependence of the conversion efficiency η, the unnormalized output of the second Kittel mode M_2, and the zero-delay second-order correlation function of the second Kittel mode $g_{22}^{(2)}(0)$ on the driving strength ξ. The values of η and M_2 described by the green dotted line and the blue dashed-dotted line, respectively, correspond to the black axis on the left. And the values of $g_{22}^{(2)}(0)$ described by the red solid line correspond to the red axis on the right. The values of the other parameters keep the same as those in Fig. 3, except for $g_{m_2c}/g_{m_1c} = 1$, $g_{qc}/g_{m_1c} = 10$, $\kappa_1/2\pi = 4$ MHz, and $\kappa_2/2\pi = 8$ MHz.

describes the population difference between the excited state and ground state of the qubit, i.e., $\hat{\sigma}_z = |e\rangle\langle e| - |g\rangle\langle g|$. Thus, the average value of σ_z can be used to characterize the degree of saturation. As illustrated in Ref. [82], the average value of σ_z ranges from 0 to -1. And when the qubit is completely saturated (i.e., the probabilities of occupying the ground state and excited state are equal), the average value of σ_z is equal to 0. When the qubit is not saturated (i.e., the qubit is in the ground state), the average value of σ_z is equal to -1. When the qubit is partially saturated, the average value of σ_z can take other values from -1 to 0. Under the weak-driving condition, the average value of σ_z can be approximately taken as -1, thus, we can obtain Eq. (9). But it is necessary to verify the rationality of this approximation from the accurate numerical perspective. As shown in Fig. 7, the average value of σ_z is plotted as a function of the driving strength ξ. We can clearly see that under the weak-driving condition, it is reasonable to approximately take the average value of σ_z as -1. And as the driving strength increases, the average value of σ_z also increases, but within the parameter range shown in this figure, its average value can still be approximated as -1.

APPENDIX B: INFLUENCE OF DRIVING STRENGTH ON THE MAGNON CONVERSION AND THE MAGNON BLOCKADE EFFECT

The weak-driving limit is a prerequisite for the implementation of our scheme, so we are interested in whether the increase of the driving strength within a certain range would make our scheme no longer applicable. In Fig. 8, we plot the conversion efficiency η, the unnormalized output of the second Kittel mode M_2, and the zero-delay second-order correlation function of the second Kittel mode $g_{22}^{(2)}(0)$ versus the driving strength ξ. With the increase of ξ, the value of $g_{22}^{(2)}(0)$ is increased, but the magnitude of its increase is very small. The value of η is almost always equal to 17.3%. But the unnormalized output of the second Kittel mode M_2 grows rapidly. When the value of $\xi/2\Pi$ approaches 1, which is still within the weak-driving range, the value of M_2 increases to $\sim$0.1. At the same time, our system can also robustly achieve magnon-mode conversion accompanied by the output of the antibunching signal.

APPENDIX C: DYNAMICAL EVOLUTION EQUATIONS AND STEADY-STATE SOLUTIONS

In Sec. III C, it is shown that the normalized zero-delay second-order correlation function $g_{22}^{(2)}(0)$ can be analytically calculated by substituting the relevant probability amplitudes C_{g01} and C_{g02} [i.e., Eqs. (16) and (17)] into Eq. (18). In this Appendix, our main aim is to provide the detailed calculation and deduction processes which are omitted in the main text but make contribution to attaining the analytical expressions of the probability amplitudes of the single- and two- magnon excitation states from the second Kittel mode [i.e., Eqs. (16a) and (16b)].

After substituting the non-Hermitian Hamiltonian $\hat{H}_{\rm tot}$ given by Eq. (7) which contains the dissipative terms and the truncated wave function $|\Psi\rangle$ expanded as Eq. (14) into the time-dependent Schrödinger equation $i\frac{\partial|\Psi\rangle}{\partial t} = \hat{H}_{\rm tot}|\Psi\rangle$, a series of dynamical evolution equations satisfied by the probability amplitudes $C_{\alpha m_1 m_2}$ can be attained as follows:

$$i\frac{\partial C_{g10}}{\partial t} = \Delta_1' C_{g10} + \xi C_{g00} + \sqrt{2}\xi C_{g20} + g_1 C_{e00} + g_m C_{g01}, \tag{C1a}$$

$$i\frac{\partial C_{g01}}{\partial t} = \Delta_2' C_{g01} + \xi C_{g11} + g_2 C_{e00} + g_m C_{g10}, \tag{C1b}$$

$$i\frac{\partial C_{g11}}{\partial t} = (\Delta_1' + \Delta_2')C_{g11} + \xi C_{g01} + g_2 C_{e10} + g_1 C_{e01} + \sqrt{2}g_m(C_{g20} + C_{g02}), \tag{C1c}$$

$$i\frac{\partial C_{g20}}{\partial t} = 2\Delta_1' C_{g20} + \sqrt{2}\xi C_{g10} + \sqrt{2}g_1 C_{e10} + \sqrt{2}g_m C_{g11}, \tag{C1d}$$

$$i\frac{\partial C_{g02}}{\partial t} = 2\Delta_2' C_{g02} + \sqrt{2}g_2 C_{e01} + \sqrt{2}g_m C_{g11}, \tag{C1e}$$

$$i\frac{\partial C_{e00}}{\partial t} = \Delta_q' C_{e00} + g_1 C_{g10} + g_2 C_{g01} + \xi C_{e10}, \tag{C1f}$$

$$i\frac{\partial C_{e10}}{\partial t} = (\Delta_1' + \Delta_q')C_{e10} + g_2 C_{g11} + \sqrt{2}g_1 C_{g20} + \xi C_{e00} + g_m C_{e01}, \tag{C1g}$$

$$i\frac{\partial C_{e01}}{\partial t} = (\Delta_2' + \Delta_q')C_{e01} + g_1 C_{g11} + \sqrt{2}g_2 C_{g02} + g_m C_{e10}, \tag{C1h}$$

where $\Delta_1' = \Delta_1 - i\frac{\kappa_1}{2}$, $\Delta_2' = \Delta_2 - i\frac{\kappa_2}{2}$, and $\Delta_q' = \Delta_q - i\frac{\gamma}{2}$.

Then in the limit of weak driving, the dynamical evolution equations can be simplified by making full use of the approximate relationship, which is expressed as Eq. (15), to neglect some terms and set $C_{g00} = 1$. Besides, through introducing the steady-state condition $i\frac{\partial C_{\alpha m_1 m_2}}{\partial t} = 0$ into Eqs. (C1a)–(C1h), a set of linear equations about the steady-state probability amplitudes $C^{ss}_{\alpha m_1 m_2}$ under the steady state $|\Psi_{ss}\rangle$ can be obtained after straightforward simplifications, which are given by

$$0 = \Delta_1' C^{ss}_{g10} + \xi + g_1 C^{ss}_{e00} + g_m C^{ss}_{g01}, \tag{C2a}$$

$$0 = \Delta_2' C^{ss}_{g01} + g_2 C^{ss}_{e00} + g_m C^{ss}_{g10}, \tag{C2b}$$

$$0 = (\Delta_1' + \Delta_2')C^{ss}_{g11} + \xi C^{ss}_{g01} + g_2 C^{ss}_{e10} + g_1 C^{ss}_{e01} + \sqrt{2}g_m C^{ss}_{g20} + \sqrt{2}g_m C^{ss}_{g02}, \tag{C2c}$$

$$0 = 2\Delta_1' C^{ss}_{g20} + \sqrt{2}\xi C^{ss}_{g10} + \sqrt{2}g_1 C^{ss}_{e10} + \sqrt{2}g_m C^{ss}_{g11}, \tag{C2d}$$

$$0 = 2\Delta_2' C^{ss}_{g02} + \sqrt{2}g_2 C^{ss}_{e01} + \sqrt{2}g_m C^{ss}_{g11}, \tag{C2e}$$

$$0 = \Delta_q' C^{ss}_{e00} + g_1 C^{ss}_{g10} + g_2 C^{ss}_{g01}, \tag{C2f}$$

$$0 = (\Delta_1' + \Delta_q')C^{ss}_{e10} + g_2 C^{ss}_{g11} + \sqrt{2}g_1 C^{ss}_{g20} + \xi C^{ss}_{e00} + g_m C^{ss}_{e01}, \tag{C2g}$$

$$0 = (\Delta_2' + \Delta_q')C^{ss}_{e01} + g_1 C^{ss}_{g11} + \sqrt{2}g_2 C^{ss}_{g02} + g_m C^{ss}_{e10}. \tag{C2h}$$

Since the above coupled algebraic equations (C2a)–(C2h) are closed, i.e., the number of the equations equals to the number of the unknown parameters, it provides the possibility to iteratively solve the analytical expressions of all the probability amplitudes under the steady state. In order to make our content more concise without compromising the completeness, we thus only provide the analytical expressions of the steady-state probability amplitudes that we are concerned about, i.e., the steady-state probability amplitudes of the single-magnon excitation state C^{ss}_{g01} and the two-magnon excitation state C^{ss}_{g02} which are shown in the main text [i.e., Eqs. (16) and (17)], while we ignore the display of other unimportant steady-state probability amplitude expressions.

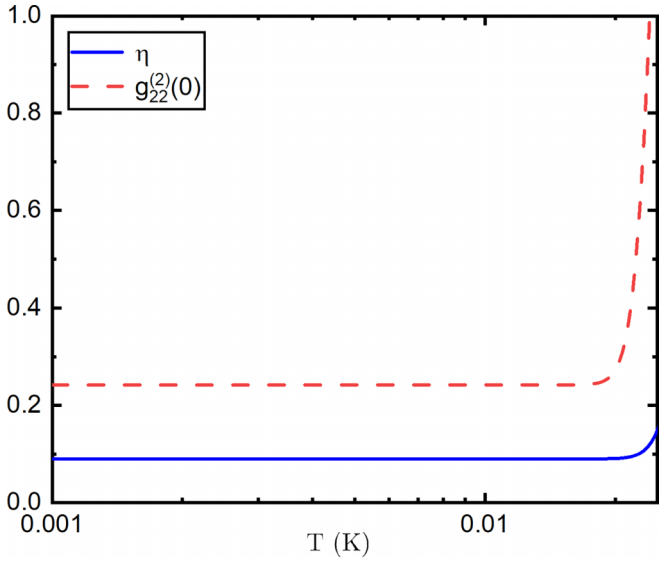

FIG. 9. Dependence of the conversion efficiency η and the zero-delay second-order correlation function of the second Kittel mode $g_{22}^{(2)}(0)$ on the ambient temperature T. The values of the other parameters keep the same as those in Fig. 3, except for $g_{m_2c}/g_{m_1c} = 1$, $g_{qc}/g_{m_1c} = 10$, and $\kappa_2/2\pi = 8$ MHz.

APPENDIX D: INFLUENCE OF TEMPERATURE ON THE MAGNON CONVERSION AND THE MAGNON BLOCKADE EFFECT

As we all know, the temperature has a significant impact on the magnon blockade effect. Therefore, we need to take the ambient temperature into account in the exact numerical simulation of the quantum master equation. The quantum master equation at temperature T is rewritten as

$$\frac{d\hat{\rho}}{dt} = -i[\hat{H}_{\rm rot}, \hat{\rho}] + \frac{\gamma}{2}\hat{\mathcal{L}}[\hat{\sigma}]\hat{\rho} + \sum_{i=1,2}\frac{\kappa_i}{2}(n_{thi}+1)\hat{\mathcal{L}}[\hat{m}_i]\hat{\rho} + \sum_{i=1,2}\frac{\kappa_i}{2}n_{thi}\hat{\mathcal{L}}[\hat{m}_i^\dagger]\hat{\rho}, \tag{D1}$$

where $n_{thi} = [\exp(\frac{\hbar\omega_{m_i}}{K_B T}) - 1]^{-1}$ is the mean thermal magnon occupation number of the ith magnon mode, $\hbar$ is the reduced Planck's constant, and K_B is Boltzmann constant. The two collapse operators $\hat{\mathcal{L}}[\hat{m}_i^\dagger]\hat{\rho}$ and $\hat{\mathcal{L}}[\hat{m}_i]\hat{\rho}$ act on the density matrix of the magnonic subsystem, for controlling the excitation and collapse of the magnons from or to the thermal reservoir, respectively, with the imbalanced efficiency $\kappa_i n_{thi}$ and $\kappa_i(n_{thi}+1)$. When the zero-temperature limit is not met, i.e., $T \neq 0$, the thermal magnons appear in the reservoir and enter into the microwave cavity, which are governed by the term $\kappa_i n_{thi}\hat{\mathcal{L}}[\hat{m}_i^\dagger]\hat{\rho}$ in the quantum master equation (D1) [97].

In Fig. 9, we plot the conversion efficiency η and the zero-delay second-order correlation function of the second Kittel mode $g_{22}^{(2)}(0)$ versus the ambient temperature T. As we tune the ambient temperature T from 1 to 16 mK, $g_{22}^{(2)}(0)$ is always equal to 0.24 and η is always equal to 0.1. When the ambient temperature T exceeds 16 mK, $g_{22}^{(2)}(0)$ starts to rapidly increase to 1. The ambient temperature T at this time

is equal to 24 mK. Under the same conditions, η increase slightly, whose reason is that the existence of $\hat{\mathcal{L}}[\hat{m}_i^\dagger]\hat{\rho}$ can act as an incoherent pump [98] and promote the microwave signal conversion between the two Kittel modes. In addition, in the current experimental works [16,22,23,44], the hybrid ferromagnet-superconductor quantum systems are placed in a dilution refrigerator at temperature of ∼10 mK. Therefore, the considered hybrid quantum system is experimentally feasible.

[1] G. Kurizki, P. Bertet, Y. Kubo, K. Molmer, D. Petrosyan, P. Rabl, and J. Schmiedmayer, Quantum technologies with hybrid systems, Proc. Natl. Acad. Sci. USA **112**, 3866 (2015).

[2] D. Lachance-Quirion, Y. Tabuchi, A. Gloppe, K. Usami, and Y. Nakamura, Hybrid quantum systems based on magnonics, Appl. Phys. Express **12**, 070101 (2019).

[3] M. Elyasi, Y. M. Blanter, and G. E. W. Bauer, Resources of nonlinear cavity magnonics for quantum information, Phys. Rev. B **101**, 054402 (2020).

[4] B. Z. Rameshti, S. V. Kusminskiy, J. A. Haigh, K. Usami, D. Lachance-Quirion, Y. Nakamura, C.-M. Hu, H. X. Tang, G. E. W. Bauer, and Y. M. Blanter, Cavity magnonics, Phys. Rep. **979**, 1 (2022).

[5] H. Y. Yuan, Y. Cao, A. Kamra, R. A. Duine, and P. Yan, Quantum magnonics: When magnon spintronics meets quantum information science, Phys. Rep. **965**, 1 (2022).

[6] M. A. Gilleo and S. Geller, Magnetic and crystallographic properties of substituted yttrium-iron garnet, $3Y_2O_3 \cdot xM_2O_3 \cdot (5-x)Fe_2O_3$, Phys. Rev. **110**, 73 (1958).

[7] A. A. Serga, A. V. Chumak, and B. Hillebrands, YIG magnonics, J. Phys. D: Appl. Phys. **43**, 264002 (2010).

[8] V. Cherepanov, I. Kolokolov, and V. Ľvov, The saga of YIG: Spectra, thermodynamics, interaction and relaxation of magnons in a complex magnet, Phys. Rep. **229**, 81 (1993).

[9] Y. Cao, P. Yan, H. Huebl, S. T. B. Goennenwein, and G. E. W. Bauer, Exchange magnon-polaritons in microwave cavities, Phys. Rev. B **91**, 094423 (2015).

[10] Y. Kajiwara, K. Harii, S. Takahashi, J. Ohe, K. Uchida, M. Mizuguchi, H. Umezawa, H. Kawai, K. Ando, K. Takanashi, S. Maekawa, and E. Saitoh, Transmission of electrical signals by spin-wave interconversion in a magnetic insulator, Nature (London) **464**, 262 (2010).

[11] X. Zhang, C.-L. Zou, L. Jiang, and H. X. Tang, Strongly coupled magnons and cavity microwave photons, Phys. Rev. Lett. **113**, 156401 (2014).

[12] Y. Tabuchi, S. Ishino, T. Ishikawa, R. Yamazaki, K. Usami, and Y. Nakamura, Hybridizing ferromagnetic magnons and microwave photons in the quantum limit, Phys. Rev. Lett. **113**, 083603 (2014).

[13] T. Neuman, D. S. Wang, and P. Narang, Nanomagnonic cavities for strong spin-magnon coupling and magnon-mediated spin-spin interactions, Phys. Rev. Lett. **125**, 247702 (2020).

[14] W. Xiong, M. Tian, G.-Q. Zhang, and J. Q. You, Strong long-range spin-spin coupling via a Kerr magnon interface, Phys. Rev. B **105**, 245310 (2022).

[15] X. Zhang, C.-L. Zou, N. Zhu, F. Marquardt, L. Jiang, and H. X. Tang, Magnon dark modes and gradient memory, Nat. Commun. **6**, 8914 (2015).

[16] D. Lachance-Quirion, Y. Tabuchi, S. Ishino, A. Noguchi, T. Ishikawa, R. Yamazaki, and Y. Nakamura, Resolving quanta of collective spin excitations in a millimeter-sized ferromagnet, Sci. Adv. **3**, e1603150 (2017).

[17] X. Zhang, C.-L. Zou, L. Jiang, and H. X. Tang, Cavity magnomechanics, Sci. Adv. **2**, e1501286 (2016).

[18] A. G. Gurevich and G. A. Melkov, *Magnetization Oscillations and Waves* (CRC Press, Boca Raton, FL, 1996).

[19] D. D. Stancil and A. Prabhakar, *Spin Waves* (Springer, Boston, 2009).

[20] S. Chakraborty and C. Das, Nonreciprocal magnon-photon-phonon entanglement in cavity magnomechanics, Phys. Rev. A **108**, 063704 (2023).

[21] D. Lachance-Quirion, S. P. Wolski, Y. Tabuchi, S. Kono, K. Usami, and Y. Nakamura, Entanglement-based single-shot detection of a single magnon with a superconducting qubit, Science **367**, 425 (2020).

[22] Y. Tabuchi, S. Ishino, A. Noguchi, T. Ishikawa, R. Yamazaki, K. Usami, and Y. Nakamura, Coherent coupling between a ferromagnetic magnon and a superconducting qubit, Science **349**, 405 (2015).

[23] Y.-P. Wang, G.-Q. Zhang, D. Xu, T.-F. Li, S.-Y. Zhu, J.-S. Tsai, and J.-Q. You, Quantum simulation of the fermion-boson composite quasi-particles with a driven qubit-magnon hybrid quantum system, arXiv:1903.12498.

[24] A. V. Chumak, V. I. Vasyuchka, A. A. Serga, and B. Hillebrands, Magnon spintronics, Nat. Phys. **11**, 453 (2015).

[25] S. Viola Kusminskiy, H. X. Tang, and F. Marquardt, Coupled spin-light dynamics in cavity optomagnonics, Phys. Rev. A **94**, 033821 (2016).

[26] J. Li, S.-Y. Zhu, and G. S. Agarwal, Magnon-photon-phonon entanglement in cavity magnomechanics, Phys. Rev. Lett. **121**, 203601 (2018).

[27] K. Ullah, M. Tahir Naseem, and Ö. E. Müstecaplioğlu, Tunable multiwindow magnomechanically induced transparency, Fano resonances, and slow-to-fast light conversion, Phys. Rev. A **102**, 033721 (2020).

[28] J. Li, S.-Y. Zhu, and G. S. Agarwal, Squeezed states of magnons and phonons in cavity magnomechanics, Phys. Rev. A **99**, 021801(R) (2019).

[29] R.-C. Shen, J. Li, Z.-Y. Fan, Y.-P. Wang, and J. Q. You, Mechanical bistability in Kerr-modified cavity magnomechanics, Phys. Rev. Lett. **129**, 123601 (2022).

[30] R. Hisatomi, A. Osada, Y. Tabuchi, T. Ishikawa, A. Noguchi, R. Yamazaki, K. Usami, and Y. Nakamura, Bidirectional conversion between microwave and light via ferromagnetic magnons, Phys. Rev. B **93**, 174427 (2016).

[31] Z.-B. Yang, X.-D. Liu, X.-Y. Yin, Y. Ming, H.-Y. Liu, and R.-C. Yang, Controlling stationary one-way quantum steering in cavity magnonics, Phys. Rev. Appl. **15**, 024042 (2021).

[32] D. Zhang, X. Q. Luo, Y. P. Wang, T. F. Li, and J. Q. You, Observation of the exceptional point in cavity magnon-polaritons, Nat. Commun. **8**, 1368 (2017).

[33] G.-Q. Zhang and J. Q. You, Higher-order exceptional point in a cavity magnonics system, Phys. Rev. B **99**, 054404 (2019).

[34] Z.-B. Yang, J.-S. Liu, H. Jin, Q.-H. Zhu, A.-D. Zhu, H.-Y. Liu, Y. Ming, and R.-C. Yang, Entanglement enhanced by Kerr nonlinearity in a cavity-optomagnonics system, Opt. Express **28**, 31862 (2020).

[35] X. Li, W.-X. Yang, T. Shui, L. Li, X. Wang, and Z. Wu, Phase control of the transmission in cavity magnomechanical system with magnon driving, J. Appl. Phys **128**, 233101 (2020).

[36] L. Bai, M. Harder, P. Hyde, Z. Zhang, C.-M. Hu, Y. P. Chen, and J. Q. Xiao, Cavity mediated manipulation of distant spin currents using a cavity-magnon-polariton, Phys. Rev. Lett. **118**, 217201 (2017).

[37] F.-X. Sun, S.-S. Zheng, Y. Xiao, Q. Gong, Q. He, and K. Xia, Remote generation of magnon Schrödinger cat state via magnon-photon entanglement, Phys. Rev. Lett. **127**, 087203 (2021).

[38] Y.-P. Wang, J. W. Rao, Y. Yang, P.-C. Xu, Y. S. Gui, B. M. Yao, J. Q. You, and C.-M. Hu, Nonreciprocity and unidirectional invisibility in cavity magnonics, Phys. Rev. Lett. **123**, 127202 (2019).

[39] X. Zhang, A. Galda, X. Han, D. Jin, and V. M. Vinokur, Broadband nonreciprocity enabled by strong coupling of magnons and microwave photons, Phys. Rev. Appl. **13**, 044039 (2020).

[40] A. Osada, R. Hisatomi, A. Noguchi, Y. Tabuchi, R. Yamazaki, K. Usami, M. Sadgrove, R. Yalla, M. Nomura, and Y. Nakamura, Cavity optomagnonics with spin-orbit coupled photons, Phys. Rev. Lett. **116**, 223601 (2016).

[41] Z.-B. Yang, J.-S. Liu, A.-D. Zhu, H.-Y. Liu, and R.-C. Yang, Nonreciprocal transmission and nonreciprocal entanglement in a spinning microwave magnomechanical system, Ann. Phys. **532**, 2000196 (2020).

[42] M. Kostylev and A. Stashkevich, Microwave to optical photon conversion by means of travelling-wave magnons in YIG films, arXiv:1712.04304.

[43] W.-J. Wu, Y.-P. Wang, J. Li, G. Li, and J. Q. You, Microwave-to-optics conversion using magnetostatic modes and a tunable optical cavity, arXiv:2403.00345.

[44] D. Xu, X.-K. Gu, H.-K. Li, Y.-C. Weng, Y.-P. Wang, J. Li, H. Wang, S.-Y. Zhu, and J. Q. You, Quantum control of a single magnon in a macroscopic spin system, Phys. Rev. Lett. **130**, 193603 (2023).

[45] S. P. Wolski, D. Lachance-Quirion, Y. Tabuchi, S. Kono, A. Noguchi, K. Usami, and Y. Nakamura, Dissipation-based quantum sensing of magnons with a superconducting qubit, Phys. Rev. Lett. **125**, 117701 (2020).

[46] M. Goryachev, W. G. Farr, D. L. Creedon, Y. Fan, M. Kostylev, and M. E. Tobar, High-cooperativity cavity QED with magnons at microwave frequencies, Phys. Rev. Appl. **2**, 054002 (2014).

[47] N. J. Lambert, J. A. Haigh, S. Langenfeld, A. C. Doherty, and A. J. Ferguson, Cavity-mediated coherent coupling of magnetic moments, Phys. Rev. A **93**, 021803(R) (2016).

[48] P.-C. Xu, J. W. Rao, Y. S. Gui, X.-F. Jin, and C.-M. Hu, Cavity-mediated dissipative coupling of distant magnetic moments: Theory and experiment, Phys. Rev. B **100**, 094415 (2019).

[49] V. L. Grigoryan and K. Xia, Cavity-mediated dissipative spin-spin coupling, Phys. Rev. B **100**, 014415 (2019).

[50] A. Imamoğlu, Cavity QED based on collective magnetic dipole coupling: Spin ensembles as hybrid two-level systems, Phys. Rev. Lett. **102**, 083602 (2009).

[51] Y. L. Ren, J. K. Xie, X. K. Li, S. L. Ma, and F. L. Li, Long-range generation of a magnon-magnon entangled state, Phys. Rev. B **105**, 094422 (2022).

[52] Y. Li, V. G. Yefremenko, M. Lisovenko, C. Trevillian, T. Polakovic, T. W. Cecil, P. S. Barry, J. Pearson, R. Divan, V. Tyberkevych, C. L. Chang, U. Welp, W.-K. Kwok, and V. Novosad, Coherent coupling of two remote magnonic resonators mediated by superconducting circuits, Phys. Rev. Lett. **128**, 047701 (2022).

[53] Z.-X. Liu, H. Xiong, and Y. Wu, Magnon blockade in a hybrid ferromagnet-superconductor quantum system, Phys. Rev. B **100**, 134421 (2019).

[54] E. Zubizarreta Casalengua, J. C. López Carreño, F. P. Laussy, and E. del Valle, Conventional and unconventional photon statistics, Laser Photon. Rev. **14**, 1900279 (2020).

[55] R. Huang, A. Miranowicz, J. Q. Liao, F. Nori, and H. Jing, Nonreciprocal photon blockade, Phys. Rev. Lett. **121**, 153601 (2018).

[56] C. Vaneph, A. Morvan, G. Aiello, M. Féchant, M. Aprili, J. Gabelli, and J. Estève, Observation of the unconventional photon blockade in the microwave domain, Phys. Rev. Lett. **121**, 043602 (2018).

[57] Y. H. Zhou, X. Y. Zhang, Q. C. Wu, B. L. Ye, Z.-Q. Zhang, D. D. Zou, H. Z. Shen, and C.-P. Yang, Conventional photon blockade with a three-wave mixing, Phys. Rev. A **102**, 033713 (2020).

[58] H. Flayac and V. Savona, Unconventional photon blockade, Phys. Rev. A **96**, 053810 (2017).

[59] M. Bamba, A. Imamoğlu, I. Carusotto, and C. Ciuti, Origin of strong photon antibunching in weakly nonlinear photonic molecules, Phys. Rev. A **83**, 021802(R) (2011).

[60] X.-W. Xu, A.-X. Chen, and Y. X. Liu, Phonon blockade in a nanomechanical resonator resonantly coupled to a qubit, Phys. Rev. A **94**, 063853 (2016).

[61] N. Didier, S. Pugnetti, Y. M. Blanter, and R. Fazio, Detecting phonon blockade with photons, Phys. Rev. B **84**, 054503 (2011).

[62] H. Xie, C.-G. Liao, X. Shang, Z.-H. Chen, and X.-M. Lin, Optically induced phonon blockade in an optomechanical system with second-order nonlinearity, Phys. Rev. A **98**, 023819 (2018).

[63] J. K. Xie, S. L. Ma, and F. L. Li, Quantum-interference-enhanced magnon blockade in an yttrium-iron-garnet sphere coupled to superconducting circuits, Phys. Rev. A **101**, 042331 (2020).

[64] Y. Xu, T. Yang, L. Lin, and J. Song, Conventional and unconventional magnon blockades in a qubit-magnon hybrid quantum system, J. Opt. Soc. Am. B **38**, 876 (2021).

[65] F. Wang, C. Gou, J. Xu, and C. Gong, Hybrid magnon-atom entanglement and magnon blockade via quantum interference, Phys. Rev. A **106**, 013705 (2022).

[66] C. Zhao, X. Li, S. Chao, R. Peng, C. Li, and L. Zhou, Simultaneous blockade of a photon, phonon, and magnon induced by a two-level atom, Phys. Rev. A **101**, 063838 (2020).

[67] X. Li, X. Wang, Z. Wu, W.-X. Yang, and A. Chen, Tunable magnon antibunching in a hybrid ferromagnet-superconductor system with two qubits, Phys. Rev. B **104**, 224434 (2021).

[68] R. Loudon, *The Quantum Theory of Light* (Oxford University Press, Oxford, 2003).

[69] K. Wu, W. X. Zhong, G. L. Cheng, and A. X. Chen, Phase-controlled multimagnon blockade and magnon-induced tunneling in a hybrid superconducting system, Phys. Rev. A **103**, 052411 (2021).

[70] R.-C. Shen, Y.-P. Wang, J. Li, S.-Y. Zhu, G. S. Agarwal, and J. Q. You, Long-time memory and ternary logic gate using a multistable cavity magnonic system, Phys. Rev. Lett. **127**, 183202 (2021).

[71] Y. Tabuchi, S. Ishino, A. Noguchi, T. Ishikawa, R. Yamazaki, K. Usami, and Y. Nakamura, Quantum magnonics: The magnon meets the superconducting qubit, C. R. Phys. **17**, 729 (2016).

[72] S. Li and A. Zhu, Perfect single-magnon generator based on a hybrid cavity-magnonic system, Ann. Phys. **534**, 2100609 (2022).

[73] H. Fröhlich, Theory of the superconducting state. I. The ground state at the absolute zero of temperature, Phys. Rev. **79**, 845 (1950).

[74] S. Nakajima, Perturbation theory in statistical mechanics, Adv. Phys. **4**, 363 (1955).

[75] Y. Wang, W. Xiong, Z. Xu, G.-Q. Zhang, and J.-Q. You, Dissipation-induced nonreciprocal magnon blockade in a magnon-based hybrid system, Sci. China Phys. Mech. Astron. **65**, 260314 (2022).

[76] Y. Fan, J. Li, and Y. Wu, Nonclassical magnon pair generation and Cauchy-Schwarz inequality violation, Phys. Rev. A **108**, 053715 (2023).

[77] Z.-B. Yang, W.-J. Wu, J. Li, Y.-P. Wang, and J. Q. You, Steady-entangled-state generation via the cross-Kerr effect in a ferrimagnetic crystal, Phys. Rev. A **106**, 012419 (2022).

[78] J. Majer, J. M. Chow, J. M. Gambetta, J. Koch, B. R. Johnson, J. A. Schreier, L. Frunzio, D. I. Schuster, A. A. Houck, A. Wallraff, A. Blais, M. H. Devoret, S. M. Girvin, and R. J. Schoelkopf, Coupling superconducting qubits via a cavity bus, Nature (London) **449**, 443 (2007).

[79] S. Filipp, M. Göppl, J. M. Fink, M. Baur, R. Bianchetti, L. Steffen, and A. Wallraff, Multimode mediated qubit-qubit coupling and dark-state symmetries in circuit quantum electrodynamics, Phys. Rev. A **83**, 063827 (2011).

[80] D. Walls and G. Milburm, *Quantum Optics* (Springer, Berlin, 1994).

[81] E. Waks and D. Sridharan, Cavity QED treatment of interactions between a metal nanoparticle and a dipole emitter, Phys. Rev. A **82**, 043845 (2010).

[82] C. Y. Hu and J. G. Rarity, Extended linear regime of cavity-QED enhanced optical circular birefringence induced by a charged quantum dot, Phys. Rev. B **91**, 075304 (2015).

[83] E. Waks and J. Vuckovic, Dipole induced transparency in drop-filter cavity-waveguide systems, Phys. Rev. Lett. **96**, 153601 (2006).

[84] C. Dong, V. Fiore, M. C. Kuzyk, and H. Wang, Optomechanical dark mode, Science **338**, 1609 (2012).

[85] Q.-u.-A. Gulfam and Z. Ficek, Highly directional photon superbunching from a few-atom chain of emitters, Phys. Rev. A **98**, 063824 (2018).

[86] G. S. Agarwal, *Quantum Optics* (Cambridge University Press, Cambridge, UK, 2013).

[87] M. O. Scully and M. S. Zubairy, *Quantum Optics* (Cambridge University, Cambridge, England, 1997).

[88] R. Rota and V. Savona, Simulating frustrated antiferromagnets with quadratically driven QED cavities, Phys. Rev. A **100**, 013838 (2019).

[89] M. H. Devoret and R. J. Schoelkopf, Superconducting circuits for quantum information: An outlook, Science **339**, 1169 (2013).

[90] J. Q. You and F. Nori, Atomic physics and quantum optics using superconducting circuits, Nature (London) **474**, 589 (2011).

[91] R. H. Brown and R. Q. Twiss, A test of a new type of stellar interferometer on sirius, Nature (London) **178**, 1046 (1956).

[92] L. De Santis, C. Antón, B. Reznychenko, N. Somaschi, G. Coppola, J. Senellart, C. Gómez, A. Lemaître, I. Sagnes, A. G. White, L. Lanco, A. Auffèves, and P. Senellart, A solid-state single-photon filter, Nat. Nanotechnol. **12**, 663 (2017).

[93] G. Zhao, Y. Wang, and X.-F. Qian, Driven dissipative quantum dynamics in a cavity magnon-polariton system, Phys. Rev. B **104**, 134423 (2021).

[94] M. P. da Silva, D. Bozyigit, A. Wallraff, and A. Blais, Schemes for the observation of photon correlation functions in circuit QED with linear detectors, Phys. Rev. A **82**, 043804 (2010).

[95] C. Lang, D. Bozyigit, C. Eichler, L. Steffen, J. M. Fink, A. A. Abdumalikov, Jr., M. Baur, S. Filipp, M. P. da Silva, A. Blais, and A. Wallraff, Observation of resonant photon blockade at microwave frequencies using correlation function measurements, Phys. Rev. Lett. **106**, 243601 (2011).

[96] P. Rabl, Photon blockade effect in optomechanical systems, Phys. Rev. Lett. **107**, 063601 (2011).

[97] Z. Liang, J. Li, and Y. Wu, All-optical polarization-state engineering in quantum cavity optomagnonics, Phys. Rev. A **107**, 033701 (2023).

[98] S. Ghosh and T. C. H. Liew, Single photons from a gain medium below threshold, Phys. Rev. B **97**, 241301(R) (2018).